CORE
Metadata, citation and similar papers at core.ac.uk
Provided by Helsingin yliopiston digitaalinen arkisto

Atomic Layer Deposition of Noble Metal Thin Films

Titta Aaltonen

Laboratory of Inorganic Chemistry
Department of Chemistry
Faculty of Science
University of Helsinki
Helsinki, Finland

Academic Dissertation

To be presented, with the permission of the Faculty of Science of the University of Helsinki, for public criticism in Auditorium A110 of the Department of Chemistry, A. I. Virtasen aukio 1, on April 8th, 2005 at 12 o'clock noon.

Helsinki 2005

Supervisors

Professor Markku Leskelä
and
Professor Mikko Ritala
Department of Chemistry
University of Helsinki
Finland

Reviewers

Professor Hyungjun Kim
Department of Materials Science and Engineering
Pohang University of Science and Technology
Korea

Professor Hannu Kattelus
VTT Information Technology
VTT Technical Research Centre of Finland
Finland

Opponent

Professor Steven George
Department of Chemistry and Biochemistry
University of Colorado
USA

© Titta Aaltonen 2005
ISBN 952-91-8460-3 (paperback)
ISBN 952-10-2390-2 (pdf version)
http://ethesis.helsinki.fi/

Yliopistopaino
Helsinki 2005

Abstract

Noble metal thin films have several potential applications for example in integrated circuits. In this work, new noble metal processes have been developed for atomic layer deposition (ALD), which is a gas phase thin film deposition method based on alternate saturative surface reactions. The self-limiting film growth mechanism of ALD leads to films with excellent conformality and good large area uniformity. In addition, the film thickness can be accurately controlled by the number of the applied growth cycles.

ALD processes for ruthenium, platinum, iridium, rhodium, and palladium were studied. All the processes are based on the reaction of the metal precursor with oxygen, the process temperatures being in the range of 200–450 °C. Metallic ruthenium films with low resistivity (< 20 $\mu\Omega\cdot$cm) and low impurity contents (< 0.2 at.% H, < 0.2 at.% C, and < 0.4 at.% O) were grown from a cyclopentadienyl precursor $RuCp_2$. Ruthenium films grown from a β-diketonato precursor $Ru(thd)_3$ had higher resistivities, higher impurity contents, and longer incubation time for onset of the film growth. High quality platinum films were grown from $MeCpPtMe_3$. The films had strong (111) orientation even at the lowest growth temperatures. Iridium films with low resistivities (< 18 $\mu\Omega\cdot$cm), low impurity contents (< 1.0 at.% H, < 0.3 at.% C, and < 0.5 at.% O), and smooth surface morphology were grown from $Ir(acac)_3$ and oxygen. Metallic rhodium films were grown from $Rh(acac)_3$ and oxygen. ALD of palladium was also studied but self-limiting film growth was not obtained.

Reaction mechanism studies were performed in order to gain better understanding of the chemistry in the studied noble metal ALD processes. It was found that adsorbed oxygen atoms react with the ligands of the noble metal precursor during the metal precursor pulse. Unreacted ligand species that remain on the surface after the metal precursor pulse react with oxygen during the following oxygen pulse. The main reaction by-products detected during the both reaction steps were water and carbon dioxide.

Preface

The research for this thesis was carried out at the Laboratory of Inorganic Chemistry, Department of Chemistry at the University of Helsinki during the years 2001–2004.

I am thankful to my supervisors Prof. Markku Leskelä and Prof. Mikko Ritala for the invaluable help and advice that I have received during this work.

I wish to thank all my co-workers for fruitful collaboration. Dr. Kai Arstila, Dr. Timo Sajavaara, Mr. Kristoffer Meinander, and Prof. Juhani Keinonen from the Department of Physics at the University of Helsinki are thanked for the TOF-ERD and AFM analysis. Mr. Raul Rammula and Prof. Väino Sammelselg from the Institute of Physical Chemistry at the University of Tartu in Estonia are thanked for the AFM analysis, and Dr. Yung-Liang Tung and Prof. Yun Chi from the Department of Chemistry at the National Tsing Huang University in Taiwan are thanked for providing the palladium precursor.

Ms. Petra Alén is thanked for her contribution to the ruthenium process, and for sharing the H-reactor, which has been a pleasure. Dr. Antti Rahtu is thanked for great help with the *in situ* experiments. All my other former and current colleagues at the Laboratory of Inorganic Chemistry are thanked as well. Special thanks belong to Marika for helping me in getting started with this work, to Marko and Raija for always being ready to help, and to Jarkko for sharing the office with me.

Mr. Seppo Nenonen (Oxford Instruments, Finland), and Dr. Thomas Moffat and Dr. Daniel Josell (National Institute of Standards and Technology, USA) are thanked for providing SEM images for this thesis.

Ms. Laura Hirvonen is thanked for revising the language of this thesis.

Finnish National Technology Agency (TEKES), ASM Microchemistry, Labgas, Fortum, Volatec, and the Academy of Finland together with Gust. Komppa Fund of Kordelin Foundation, Hämäläisten Ylioppilassäätiö, and Nokia Foundation are acknowledged for the financial support of this work.

List of publications

The thesis is based on the following original publications, which are referred to in the text by the Roman numerals I–VIII.

I T. Aaltonen, P. Alén, M. Ritala, and M. Leskelä,
Ruthenium Thin Films Grown by Atomic Layer Deposition,
Chem. Vap. Deposition, **9** (2003) 45–49.

II T. Aaltonen, M. Ritala, T. Sajavaara, J. Keinonen, and M. Leskelä,
Atomic Layer Deposition of Platinum Thin Films,
Chem. Mater., **15** (2003) 1924–1928.

III T. Aaltonen, A. Rahtu, M. Ritala, and M. Leskelä,
Reaction Mechanism Studies on Atomic Layer Deposition of Ruthenium and Platinum, *Electrochem. Solid-State Lett.*, **6** (2003) C130–C133.

IV T. Aaltonen, M. Ritala, K. Arstila, J. Keinonen, and M. Leskelä,
Atomic Layer Deposition of Ruthenium Thin Films from $Ru(thd)_3$ and Oxygen,
Chem. Vap. Deposition, **10** (2004) 215–219.

V T. Aaltonen, M. Ritala, V. Sammelselg, and M. Leskelä,
Atomic Layer Deposition of Iridium Thin Films,
J. Electrochem. Soc., **151** (2004) G489–G492.

VI T. Aaltonen, M. Ritala, Y.-L. Tung, Y. Chi, K. Arstila, K. Meinander, and M. Leskelä, Atomic Layer Deposition of Noble Metals: Exploration of the Low Limit of the Deposition Temperature, *J. Mater. Res.*, **19** (2004) 3353–3358.

VII T. Aaltonen, M. Ritala, and M. Leskelä,
Atomic Layer Deposition of Rhodium Thin Films from $Rh(acac)_3$ and Oxygen,
manuscript.

VIII T. Aaltonen, M. Ritala, and M. Leskelä,
Atomic Layer Deposition of Noble Metals,
in *Advanced Metallization Conference 2004 (AMC 2004)*, (Eds: D. Erb, P. Ramm, K. Masu, and A. Osaki), Materials Research Society (2005) 663–667.

List of symbols and abbreviations

k	relative dielectric constant, relative permittivity (ε_r)
θ	angle between the incident X-ray beam and the substrate surface
acac	2,4-pentanedionato, acetylacetonato, $[CH_3C(O)CHC(O)CH_3]^-$
AFM	atomic force microscopy
ALD, ALE	atomic layer deposition, atomic layer epitaxy
BLT	$(Bi,La)_4Ti_3O_{12}$
BST	$(Ba,Sr)TiO_3$
CMOS	complementary metal-oxide-semiconductor
CMP	chemical mechanical polishing
Cp	cyclopentadienyl, $[C_5H_5]^-$
DRAM	dynamic random access memory
EDX, EDS	energy dispersive X-ray spectroscopy
Et	ethyl, $-CH_2CH_3$
fcc	face-centered cubic
FET	field effect transistor
FRAM	ferroelectric random access memory
hfac	1,1,1,5,5,5-hexafluoro-2,4-pentanedionato, hexafluoroacetylacetonato, $[CF_3C(O)CHC(O)CF_3]^-$
hcp	hexagonal close packed
IC	integrated circuit
keim2	$[CF_3C(O)CHC(NBu^n)CF_3]^-$
Me	methyl, $-CH_3$
MFIS	metal-ferroelectric-insulator-semiconductor
MFMIS	metal-ferroelectric-metal-insulator-semiconductor
MOSFET	metal-oxide-semiconductor field effect transistor
MRAM	magnetic random access memory
od	2,4-octanedionato, $[CH_3C(O)CHC(O)CH_2CH_2CH_2CH_3]^-$
PEALD	plasma enhanced atomic layer deposition
PLZT	$(Pb,La)(Zr,Ti)O_3$
poly-Si	polycrystalline silicon
PZT	$Pb(Zr,Ti)O_3$
QCM	quartz crystal microbalance
QMS	quadrupole mass spectrometer

RF-ID	radio frequency identification
RHEED	reflection high energy electron diffraction
RIE	reactive ion etching
rms	root mean quare
RT	room temperature
SAM	self-assembled monolayer
sccm	standard cubic centimeters per minute
SEM	scanning electron microscopy
SBT	$SrBi_2Ta_2O_9$
TEM	transmission electron microscopy
thd	2,2,6,6-tetramethyl-3,5-heptanedionato, dipivaloylmethanato, $[(CH_3)_3CC(O)CHC(O)C(CH_3)_3]^-$
TOF-ERDA	time-of-flight elastic recoil detection analysis
UHV	ultra high vacuum
XPS	X-ray photoelectron spectroscopy
XRD	X-ray diffraction
XRR	X-ray reflectivity

Contents

Abstract 3

Preface 4

List of publications 5

List of symbols and abbreviations 6

Contents 8

1. Introduction 10

1.1 Noble metals 11

1.2 Atomic layer deposition 13

2. Applications of noble metals 14

2.1 Dynamic random access memory electrodes 15

2.1.1 Electrodes for Ta_2O_5 17

2.1.2 Electrodes for $(Ba,Sr)TiO_3$ 18

2.2 Ferroelectric random access memory electrodes 21

2.2.1 Electrodes for $Pb(Zr,Ti)O_3$ 22

2.2.2 Electrodes for $SrBi_2Ta_2O_9$ 24

2.2.3 Electrodes for $(Bi,La)_4Ti_3O_{12}$ 25

2.3 Gate electrodes in metal-oxide-semiconductor field effect transistors 25

2.4 Copper seed layers and barriers in interconnect metallization 27

3. Experimental methods 30

3.1 Film growth 30

3.2 Film characterization 30

3.2.1 X-ray diffraction and X-ray reflectivity 31

3.2.2 Scanning electron microscopy and energy dispersive X-ray spectroscopy 32

3.2.3 Atomic force microscopy 33

3.2.4 Time-of-flight elastic recoil detection analysis 34

3.2.5 Electrical measurements 35

4. ALD of noble metals **36**
4.1 Film growth 37
4.1.1 Ruthenium 37
4.1.2 Platinum 43
4.1.3 Iridium 46
4.1.4 Palladium 48
4.1.5 Rhodium 51
4.2 Reaction mechanisms 52
4.2.1 Oxidizing processes 52
4.2.2 Reducing processes 56

5. Conclusions **58**

6. References **60**

1. INTRODUCTION

Atomic layer deposition (ALD), also called atomic layer epitaxy (ALE), is a thin film deposition technique developed in Finland in the mid 1970s.[1] Initially, ALD was developed for deposition of materials used in electroluminescent displays[2–4] but during the years, the selection of materials and their potential applications has expanded. For instance, ALD of epitaxial compound semiconductors,[5,6] catalysts,[7,8] and sensor materials[9] has been studied. Recently, there has been a rapidly growing interest in ALD of materials used in microelectronic applications, especially in the integrated circuits (ICs).[4,10]

ICs are used in numbers of electronic devices; they can for example be found in personal computers, mobile phones, radios, and cars. The performance of the ICs is continuously improved by scaling down the dimensions of the components and by using better materials. This sets new requirements for the processes used in fabrication of the ICs; very thin films of novel materials need to be grown into three-dimensional structures. ALD produces films with excellent conformality and good thickness uniformity,[11] and is therefore a suitable thin film deposition method for IC applications. There has been a lot of research on ALD of high dielectric constant (high-*k*) oxides such as HfO_2, ZrO_2, Al_2O_3, Ta_2O_5 and their nanolaminates for gate dielectrics in the metal-oxide-semiconductor field effect transistors (MOSFETs).[4,10] There are also several reports on ALD of tantalum, titanium, and their nitrides, which are used as adhesion promoters and diffusion barriers for copper.[12] ALD of tungsten[13] and copper,[14,15] both of which are being used in interconnect metallization, have also been studied. Until very recently, there have been only a few studies on ALD of noble metals although they also have several potential applications in ICs.

Noble metals are chemically very stable, and many of them can withstand highly oxidizing conditions. Therefore, noble metals are applicable to ICs as electrodes in dynamic random access memories (DRAMs) and ferroelectric random access memories (FRAMs). Other applications in ICs include gate electrodes in MOSFETs, and seed and barrier layers for copper in interconnect metallization. In addition to ICs, noble metals have applications for example in catalysis, sensors, and magnetic data storage.

The aim of this work was to develop new ALD processes for the noble metals to be used in the above mentioned applications. Reaction mechanisms of selected processes were studied to obtain better understanding of the chemistry these processes involve. In this thesis, first there is a brief introduction to the noble metals and to the ALD technique.

Then, some of the potential applications of the noble metals are presented, the focus being on the ICs. The experimental section describes the experimental set-up used in the film growth studies as well as in the *in situ* experiments, and briefly presents the film characterization methods. After that, the so far studied noble metal ALD processes are reviewed and the reaction mechanisms of the processes discussed.

1.1 Noble metals

In this work, the following metals are counted as noble metals: silver and gold, and the platinum group metals ruthenium, rhodium, palladium, osmium, iridium, and platinum. These metals are in some contexts, especially in jewelry, also referred to as precious metals. They are transition metals and belong to groups 8–11 in the periodic table (Figure 1). Noble metals are called 'noble' because of their chemical stability; they have positive standard reduction potentials,[16] and many of them are highly resistant to oxidation, even at elevated temperatures.[17–19]

1																	18
1 H	2											13	14	15	16	17	2 He
3 Li	4 Be											5 B	6 C	7 N	8 O	9 F	10 Ne
11 Na	12 Mg	3	4	5	6	7	8	9	10	11	12	13 Al	14 Si	15 P	16 S	17 Cl	18 Ar
19 K	20 Ca	21 Sc	22 Ti	23 V	24 Cr	25 Mn	26 Fe	27 Co	28 Ni	29 Cu	30 Zn	31 Ga	32 Ge	33 As	34 Se	35 Br	36 Kr
37 Rb	38 Sr	39 Y	40 Zr	41 Nb	42 Mo	43 Tc	44 Ru	45 Rh	46 Pd	47 Ag	48 Cd	49 In	50 Sn	51 Sb	52 Te	53 I	54 Xe
55 Cs	56 Ba	*	72 Hf	73 Ta	74 W	75 Re	76 Os	77 Ir	78 Pt	79 Au	80 Hg	81 Tl	82 Pb	83 Bi	84 Po	85 At	86 Rn
87 Fr	88 Ra	**	104 Rf	105 Db	106 Sg	107 Bh	108 Hs	109 Mt	110 Ds	111 Rg	112 Uub	113 Uut	114 Uuq	115 Uup			
		*	57 La	58 Ce	59 Pr	60 Nd	61 Pm	62 Sm	63 Eu	64 Gd	65 Tb	66 Dy	67 Ho	68 Er	69 Er	70 Yb	71 Lu
		**	89 Ac	90 Th	91 Pa	92 U	93 Np	94 Pu	95 Am	96 Cm	97 Bk	98 Cf	99 Es	100 Fm	101 Md	102 No	103 Lr

Figure 1. Position of the noble metals in the periodic table. Noble metals include ruthenium (Ru), rhodium (Rh), palladium (Pd), silver (Ag), osmium (Os), iridium (Ir), platinum (Pt), and gold (Au).

Table 1 presents the atomic and physical properties of the noble metals.[20,21] The melting points of the noble metals vary from 962 °C for silver to 3033 °C for osmium. The densities are in the range of 10.5–22.6 g/cm^3. Silver has the resistivity of 1.5 $\mu\Omega$·cm, which is the lowest of all the metals. The vacuum work functions are in the range of 4.7–5.9 eV, the lowest value being for ruthenium and the highest values for osmium and platinum.[20] Ruthenium and osmium have the hexagonal close packed (hcp) crystal structure while rhodium, iridium, palladium, platinum, and gold are face-centered cubic (fcc) metals. Silver has normally the fcc crystal structure but the hcp structure has also been reported for silver.[21]

Table 1. Atomic and physical properties of the noble metals.[20,21]

Metal	**Atomic number**	**Atomic weight (*u*)**	**Melting point (°C)**	**Density at 25 °C (g/cm^3)**	**Resistivity at 0 °C ($\mu\Omega$·cm)**	**Work function (eV)**	**Crystal structure**
Ru	44	101.07	2334	12.1	7.1	4.71[a]	hcp
Os	76	190.23	3033	22.6	8.1	5.93[a]	hcp
Rh	45	102.91	1964	12.4	4.3	4.98[a]	fcc
Ir	77	192.22	2446	22.5	4.7	5.76[b]	fcc
Pd	46	106.42	1555	12.0	9.8	5.22[a] 5.6[b]	fcc
Pt	78	195.08	1768	21.5	9.6	5.64[a] 5.93[b]	fcc
Ag	47	107.87	962	10.5	1.5	4.74[b]	fcc (hcp)
Au	79	196.97	1064	19.3	2.0	5.31[b]	fcc

[a]polycrystalline, [b](111) oriented

1.2 Atomic layer deposition

ALD is a gas phase thin film deposition method which can be regarded as a special modification of the more widely used chemical vapor deposition (CVD) technique. In ALD, the precursors are led into the reaction chamber in alternate pulses while in CVD, the precursors are led into the reaction chamber simultaneously. The alternate precursor pulses in ALD are separated by inert gas purging (in flow type reactors) or by evacuation of the reactor (in high-vacuum type reactors). The precursors react with the surface groups on the substrate, or chemisorb on the substrate surface. In properly chosen process conditions, the surface reactions are self-limiting, which leads to highly controlled film growth. Thermal self-decomposition of the precursors destroys the self-limiting film growth mechanism, and the process can no longer be considered an ideal ALD process.[4] If the surface reactions become saturated, a constant film growth rate is obtained over the whole substrate surface, and films with excellent conformality and good large-area uniformity are obtained.[11] The set of successive pulses of two or more precursors, separated by purge periods, is called an ALD cycle. The film growth rate is usually measured as the film thickness obtained during one ALD cycle. The film thickness can be easily and accurately controlled by the number of the applied growth cycles.[4]

2. APPLICATIONS OF NOBLE METALS

Noble metals have several applications because of their catalytic, chemical, optical, magnetic, mechanical, and electrical properties. In many applications, only a thin, less than 1 μm thick noble metal layer is needed. The catalytic activity of noble metals is widely exploited in production or disposal of different chemical compounds. Noble metals are used as catalysts in hydrocarbon conversion reactions[22–26] and in production of other industrial chemicals such as ammonia.[27] Platinum, palladium, and rhodium are used as three-way catalysts in automobile catalytic converters,[28] and iridium, platinum, and silver have been studied as catalysts for reduction of nitric oxide exhausted from diesel and lean-burn gasoline engines.[29,30] The catalytic activity of the noble metals is also exploited in fuel cell technology; rhodium, ruthenium, palladium, platinum, and gold have been studied as catalysts for production of carbon monoxide free hydrogen for fuel cells,[31,32] and platinum and its alloys with other noble metals have been studied as fuel cell electrode catalysts.[33–35] Liquid phase techniques are the most common methods used for preparation of the noble metal catalysts but gas phase methods can be used as well.[23,27,36] ALD is a suitable gas phase method for catalyst preparation because ALD is based on controlled adsorption of the precursors on the growth surface.[7,8] Thus, precise surface structures can be prepared on the catalyst supports. In addition, excellent dispersion and distribution of metal species can be obtained by ALD, the processes being highly reproducible.[8] ALD of palladium, ruthenium, iridium, and platinum on high surface area supports for catalytic applications have been reported recently.[37–39]

The optical, mechanical, and chemical properties of noble metals are exploited in optical and protective coatings,[40–42] and permeation of hydrogen through noble metals is exploited in hydrogen separation membranes.[43,44] In gas sensor applications, noble metals have been used for example as active electrode materials[45–47] and as catalytic layers which selectively remove specific gas species, thus prohibiting their access to the active sensor surface.[48]

The applications of noble metals in magnetic data storage include antiferromagnetically coupled magnetic recording media[49,50] and magnetic random access memories (MRAMs).[51,52] The antiferromagnetically coupled magnetic recording media consists of two or more ferromagnetic layers separated by a ruthenium film. The role of the nonmagnetic ruthenium film is to antiferromagnetically couple the ferromagnetic layers, and thus stabilize the magnetic orientation of the information-storing magnetic layer.[49,50] In magnetic tunneling junction MRAMs, the antiferromagnetic coupling stabilizes the

magnetic orientation of the fixed magnetic layer.[51,52] In addition to ruthenium, iridium has been studied as a nonmagnetic coupling layer but it suffers from a poor thermal stability with the adjacent magnetic layers.[53] The degree of the antiferromagnetic coupling depends on the thickness of the nonmagnetic film, the optimum thickness for ruthenium being in the range of 0.6–0.8 nm.[49] Thus, an accurate thickness control of the deposited films is needed over the whole substrate area. Sputtering has been so far used for deposition of the ruthenium films[49,51] but ALD as well could be a suitable method for ruthenium deposition for these applications.

Noble metals have several potential applications in ICs. They can be used as electrodes in DRAMs and FRAMs, and as gate electrodes in MOSFETs. In addition, noble metals have been studied as diffusion barriers and seed layers for copper in interconnect metallization. These applications of the noble metals in ICs are described in more detail in the following sections.

2.1 Dynamic random access memory electrodes

The data storage in DRAMs is based on introducing a charge into the memory capacitor. The charge must be repeatedly refreshed (thereof the term 'dynamic'), the time interval between the refreshments depending on the leakage current through the capacitor. The charge storage capacity of the capacitor is determined by its capacitance, which can be increased by decreasing the thickness of the dielectric layer, by using a dielectric material with a higher dielectric constant, or by increasing the active capacitor area.[54] Three-dimensional structures provide larger capacitor areas even if the lateral dimensions of the capacitors decrease, and therefore, three-dimensional structures are needed in order to further increase the number of capacitors per unit area, and thus, the storage density of the DRAMs.[55–57] In stacked DRAM memory cells, the capacitors are fabricated above the silicon substrate.[56,58] Examples of stacked capacitor structures are shown in Figure 2. In trenched DRAM memory cells, the memory capacitors are buried into the silicon substrate. The capacitors are fabricated into high aspect ratio trenches, and thus have high effective surface areas.[58,59] The area of the trench can be further increased by making it for example bottle-shaped.[59]

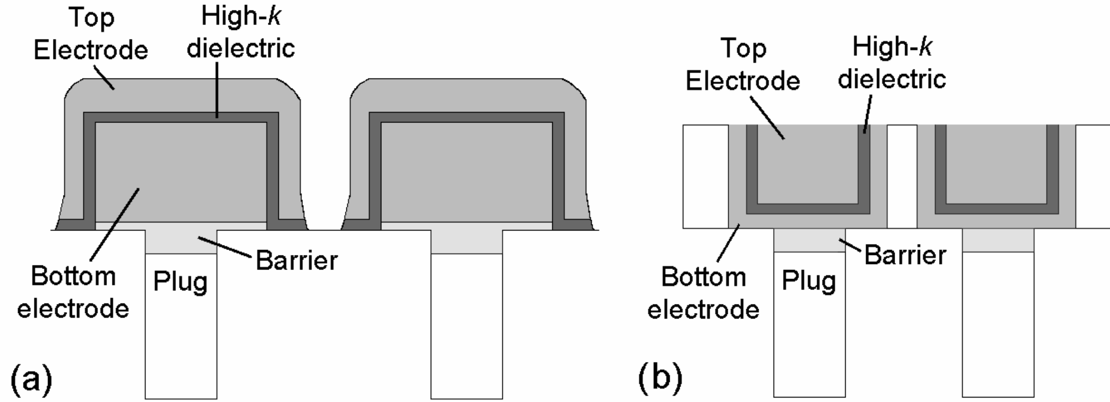

Figure 2. (a) An example of a simple stacked DRAM capacitor structure, and (b) an example of a concave stacked DRAM capacitor structure.

There is active research on high-*k* materials that could replace the currently used dielectrics SiO_2 and silicon oxynitride composites. Examples of widely studied high-*k* oxides include Ta_2O_5 and $(Ba,Sr)TiO_3$ (BST).[55,58,60,61] These high-*k* oxides cannot be grown directly on the polycrystalline silicon (poly-Si) plug that connects the memory capacitor to the cell transistor because the plug would oxidize during the high-*k* oxide processing, and oxidation of the plug would lead to a decrease in the total capacitance of the structure.[62] Therefore, a bottom electrode that prevents the plug oxidation and that remains conductive at highly oxidizing conditions is needed. Noble metals platinum, iridium, and ruthenium, and conductive oxides RuO_2, IrO_2, and $SrRuO_3$ are potential electrode materials for DRAM memory capacitors having high-*k* dielectrics.[61] Noble metals are suitable electrode materials because they remain conductive in highly oxidizing conditions; platinum is highly resistant to oxidation, whereas iridium and ruthenium form conductive oxides (IrO_2 and RuO_2) when they become oxidized.[61] Furthermore, noble metals have high work functions, and thus high barrier for leakage by Schottky emission, that is, thermionic emission in the presence of an applied electric field.[61]

Patterning is an essential process step in fabrication of the three-dimensional DRAM capacitor structures. Patterning of the stacked capacitors (Figure 2) can be realized by vertical dry etching through a hard mask,[54,63–65] or by planarization.[66,67] The most common dry etching method used in patterning of the noble metals is reactive ion etching (RIE). RIE of platinum and iridium is difficult because they do not have readily generated volatile etch products at low temperatures.[54] Sputtering, which in the lack of chemical reactions becomes the predominant etching mechanism in RIE, decreases selectivity between the metal and the mask, and may cause re-deposition of the metal on the pattern sidewall.[55,68]

By using a hard mask that tolerates elevated temperatures and more aggressive etching conditions, higher quality RIE of platinum and iridium can be obtained.[55,65,68,69] RIE of ruthenium and RuO_2 is easier because they react readily with Cl_2 containing O_2 plasma, or with CF_4 plasma to form volatile ruthenium oxides and halides.[55,63,64,70] The drawback with RIE of ruthenium with O_2 plasma is that the reaction product RuO_4 is toxic. Planarization of the capacitor structures is done by chemical mechanical polishing (CMP). Both stacked and trenched structures can be planarized by CMP.[59,66,67] In general, CMP of noble metals is difficult because of their chemical inactivity. Thus, there are only a few reports on CMP of iridium,[66] platinum,[71,72] and ruthenium.[67]

The bottom electrode affects the dielectric and electrical properties of the high-*k* oxide, and plays therefore a significant role in the performance of the memory capacitor.[61,73,74] The following sections summarize the noble metal electrode structures studied for DRAM capacitors with Ta_2O_5 and BST as the dielectric materials.

2.1.1 Electrodes for Ta_2O_5

Ruthenium is a potential bottom electrode material for capacitors with Ta_2O_5 as the dielectric because high dielectric constants and low leakage currents have been reported for Ta_2O_5 grown on ruthenium electrodes.[74,75] For crystalline Ta_2O_5 films, dielectric constants in the range of 45–110[76,77] have been reported whereas for amorphous films, the dielectric constant is about 25–32.[77] Thus, in order to obtain higher dielectric constants, the Ta_2O_5 films need to be crystallized. The crystallization is usually performed by post-annealing at a temperature of 700 °C or higher.[74,75] If the high-temperature annealing is performed in an O_2 atmosphere, the ruthenium bottom electrode is likely to become oxidized to ruthenium oxide. The RuO_2 formation causes roughening of the Ta_2O_5–electrode interface which leads to higher leakage currents.[75,78] Therefore, in order to prevent ruthenium oxidation, the high-temperature annealing of Ta_2O_5 is usually performed in a N_2 atmosphere or in vacuum.[75,77] The dielectric properties of Ta_2O_5 can also be improved by O_2 or N_2O plasma treatments or O_2 annealing performed at lower temperatures of 350–550 °C at which oxidation of the ruthenium bottom electrode does not take place.[74,75,77]

Platinum is another bottom electrode material studied for Ta_2O_5.[74,76] Platinum is more resistant to oxidation and can therefore be high-temperature annealed in an O_2 atmosphere.[74] However, oxygen readily diffuses through platinum and oxidizes the contact beyond the platinum layer. Furthermore, etching of platinum is difficult.[54]

The crystal structure of the bottom electrode affects crystallization of the Ta_2O_5 film and thus its electrical properties.[74] Ta_2O_5 films with (110)[74] and (200)[76] orientations have been obtained on (111) oriented platinum films. Ta_2O_5 films with a slightly preferred (001) orientation have been obtained on randomly oriented ruthenium films,[74] while Ta_2O_5 films with a highly dominant (001) orientation and a very high dielectric constant of 90–110 have been obtained on (002) oriented ruthenium electrodes.[77] The high dielectric constant of the Ta_2O_5 film is suggested to be caused by the strong (001) orientation of the Ta_2O_5 film[77,79] brought out by the (002) orientation of the ruthenium bottom electrode.[74] Thus, ruthenium films with (002) crystal orientation can be considered the most suitable bottom electrodes for DRAMs with Ta_2O_5 as the capacitor dielectric.

2.1.2 Electrodes for $(Ba,Sr)TiO_3$

BST is a promising dielectric material for DRAM capacitors because of its high dielectric constant (> 200).[61] Furthermore, low leakage currents can be obtained with BST.[61] High-temperature (> 500 °C) deposition or post-annealing is needed to obtain the desired perovskite crystal structure of the BST films.[56,73] Platinum, ruthenium, and iridium are suitable electrode materials for BST because they remain conductive in the highly oxidizing deposition and annealing conditions needed for BST processing.[61]

Platinum has been widely studied as electrode material for BST because very low leakage currents have been obtained with BST grown on platinum electrodes.[56,61,73] The low leakage currents are due to a high potential barrier at the BST–platinum interface; platinum has a high work function, and thus a high barrier for leakage by Schottky emission.[61,80,81] Another reason for the low leakage currents is that smooth platinum–BST interfaces can be obtained because platinum is highly resistant to oxidation,[61,73,82,83] and no oxidation related surface roughening takes place during BST processing. However, poor electrical quality of the BST–platinum top electrode interface may lead to higher leakage currents at negative bias.[61,84]

Platinum cannot be grown directly on the poly-Si plug because it reacts with poly-Si to form platinum silicide.[54,85] In addition, adhesion of platinum to poly-Si is poor.[62] Therefore, a conductive barrier layer that prevents silicide formation and enhances adhesion is needed between the poly-Si plug and the platinum electrode.[54] However, a simple BST/platinum/barrier/poly-Si structure cannot be used because platinum is highly permeable to oxygen. Diffusion of oxygen through platinum leads to oxidation of the

underlying barrier and plug materials during BST processing.[54,82,85] The problem with oxygen permeability can be overcome by using an electrode stack consisting of a platinum layer together with an additional oxygen barrier layer that has lower permeability for oxygen. Potential oxygen barrier materials include for example ruthenium, iridium, RuO_2, and IrO_2.[54,62,82,85]

Ruthenium is another electrode material that has been studied for DRAMs with BST as the dielectric. BST films grown on (002) oriented ruthenium electrodes have been reported to have a strong (110) crystal orientation and a large grain size, and thereby, a high dielectric constant.[73,86] Ruthenium is less stable towards oxidation than platinum; the surface of the ruthenium electrode oxidizes to ruthenium oxide during BST deposition at temperatures of 500 °C and higher.[73,86,87] The surface oxide attenuates oxygen diffusion through the ruthenium electrode, and thus retards the oxidation of the underlying plug material.[82,87,88] However, the surface oxidation also causes roughening of the ruthenium–BST interface leading to high leakage currents.[89,90] The ruthenium electrode can be processed by special annealings or plasma treatments to lower the leakage current.[82,91,92] The potential barrier at the BST–ruthenium (or RuO_2) interface is lower than at the BST–platinum and BST–iridium interfaces, which is another reason for higher leakage currents obtained for BST films grown on ruthenium electrodes.[61]

The ability of ruthenium to retard oxygen diffusion can be exploited in multilayer structures such as BST/Pt/Ru/TiN/poly-Si. The ruthenium layer attenuates oxidation of the nitride barrier and the poly-Si plug, while smooth surface morphology is preserved at the platinum–BST interface, and thus, lower leakage currents are obtained.[82] Ruthenium can also be grown directly on the poly-Si plug without the need for a separate barrier layer.[93] Ruthenium reacts with silicon to form Ru_2Si_3 at temperatures higher than 450 °C,[85,86] but in specific process conditions, a conductive ruthenium, silicon, and oxygen containing layer that is stable up to 700 °C can be obtained at the ruthenium–poly-Si interface.[93] However, the stability of the ruthenium–poly-Si interface during back-end processing remains a question.[56]

Iridium is a promising electrode material for BST because good dielectric properties have been reported for BST films grown on iridium electrodes.[73,94,95] BST films having a preferred crystal orientation, and therefore, a high dielectric constant, have been obtained on iridium electrodes.[95] The top electrode material affects the dielectric constant of the BST film as well; higher dielectric constants have been obtained when iridium is used as

the top electrode instead of platinum.[95] This difference was explained by a large compressive stress in the BST film induced by the iridium top electrode. The leakage currents reported for BST films grown on iridium are, however, higher than for BST films grown on platinum.[73,94] High-temperature post-annealing in O_2 atmosphere has been reported to lower the leakage currents of BST films grown on iridium electrodes.[73]

An iridium oxide layer forms on the surface of the iridium electrode during BST processing at temperatures of 600 °C or higher.[85,95,96] This iridium oxide layer can act as an oxygen diffusion barrier.[95] Iridium films annealed at 700 °C in N_2 atmosphere have been reported to prevent oxygen diffusion better than non-annealed films.[85] This is because the number of grain boundaries reduces during the high temperature annealing. Thus, there are less pathways for oxygen diffusion.[85] The stability of iridium in contact with silicon is moderate; iridium reacts with silicon when annealed in O_2 atmosphere at 650 °C but is not completely consumed in the reaction with silicon.[97]

In summary, platinum, ruthenium, and iridium are the most widely studied noble metal electrode materials for BST. Platinum has good interface stability with BST but the oxygen permeability of platinum is a problem. Formation of a thin oxide layer on the surface of the ruthenium and iridium electrodes retards further oxygen diffusion. However, surface roughening of the ruthenium electrodes as a result of the surface oxidation leads to high leakage currents. Therefore, multilayer structures consisting of several noble metal layers show most promise as bottom electrodes for BST.

Highly conformal noble metal thin films are needed in fabrication of three-dimensional DRAM capacitor structures. Therefore, ALD and CVD are suitable methods for noble metal deposition for DRAMs.[57] Films grown by physical methods such as sputtering, on the other hand, suffer from poor step coverage.[98] The noble metal layer grown on top of the nitride barrier should be grown by a reductive process in order to avoid oxidation of the barrier during the noble metal deposition. The subsequent bottom electrode layers as well as the top electrode can be grown by oxidizing processes as well.

2.2 Ferroelectric random access memory electrodes

In FRAMs, the data is stored as the polarization state of the ferroelectric film. Switching between two stable polarization states is realized by applying an electric field across the ferroelectric film. As both of the polarization states are stable in the absence of electric field, FRAMs are non-volatile, that is, the data is preserved when the power is switched off.[99] In addition to non-volatility, the benefits of FRAMs include fast reading and writing times, low power consumption, and low operation voltage.[100,101] Therefore, FRAMs are applicable to portable electronics such as mobile phones, and to other wireless applications such as radio frequency identification (RF-ID) cards and smart IC cards.[100–102]

FRAMs have two different types of operation principles; the data can be stored in ferroelectric capacitors or in ferroelectric transistors. Ferroelectric capacitors are otherwise similar to DRAM capacitors (Figure 2) but the high-*k* dielectric is replaced by the ferroelectric film. In ferroelectric capacitors, an excess charge is drawn from the circuit and stored to the capacitor if the polarization state of the ferroelectric film is changed during the read-out process. Thus, the polarization state of the ferroelectric film can be determined by detecting the presence or the absence of the switching charge pulse.[99] The magnitude of the switching charge can be increased by using three-dimensional capacitor structures.[103] The metal-ferroelectric-insulator-semiconductor (MFIS) FET[104] shown in Figure 3 is an example of a ferroelectric transistor. In ferroelectric transistors, the conductance of the transistor channel depends on the polarization state of the gate ferroelectric. The polarization state of the ferroelectric film can thus be determined by measuring the drain current.[105,106] The advantage of the ferroelectric transistors is that unlike in the ferroelectric capacitors, the data read-out is non-destructive.

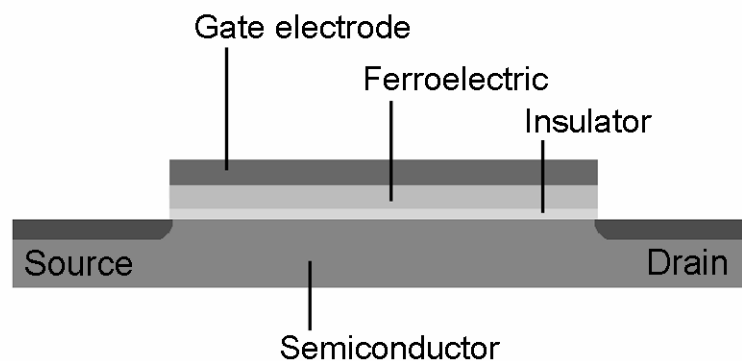

Figure 3. A schematic of a MFIS field effect transistor.

$Pb(Zr,Ti)O_3$ (PZT), $SrBi_2Ta_2O_9$ (SBT), and $(Bi,La)_4Ti_3O_{12}$ (BLT) are widely studied ferroelectrics for FRAMs.[101,104,107] In ferroelectric capacitors, the bottom electrode affects the texture and quality, and thereby the performance of the ferroelectric film.[101] Since the ferroelectric oxides are deposited in oxidizing conditions and at high temperatures of 450–850 °C,[101] bottom electrodes that remain conductive in these process conditions are needed. Therefore, noble metals platinum, iridium, and ruthenium as well as their conductive oxides IrO_2 and RuO_2 are potential electrode materials for FRAM capacitors.

In ferroelectric transistors, noble metals are used as gate electrodes. In a MFIS transistor (Figure 3), the electrode is grown on top of the ferroelectric material while in a metal-ferroelectric-metal-insulator-semiconductor (MFMIS) transistor the ferroelectric is grown on the metal electrode. Noble metals platinum, iridium and ruthenium have been studied as gate metals in the ferroelectric gate transistors.[104,108,109] The following sections summarize the noble metal electrode structures studied for FRAM capacitors and FRAM transistors having PZT, SBT, or BLT as the ferroelectric.

2.2.1 Electrodes for $Pb(Zr,Ti)O_3$

PZT and lanthanum substituted PZT [$(Pb,La)(Zr,Ti)O_3$, PLZT] are widely studied ferroelectric materials in FRAM memory capacitors. Processing of the PZT films is performed in oxidizing conditions at temperatures of 450–700 °C.[101] A disadvantage with PZT is that it is prone to fatigue; the switching polarization of PZT decreases with increasing number of repeated reading and writing cycles.[101,106,110] However, fatigue problems with PZT can be overcome by tailoring the electrode structure.[101] Diffusion of hydrogen through the electrode to PZT film during later device processing degrades its ferroelectric properties.[101,111] Therefore, the top electrode needs to be covered by an additional hydrogen barrier layer. Alternatively, a top electrode material such as IrO_2, which has low catalytic activity for dissociation of H_2 to hydrogen atoms, can be used.[101,111]

Platinum is a widely studied electrode material for PZT. A multilayer electrode stack is always needed when using platinum electrodes because platinum reacts with poly-Si to form platinum silicide,[85] is permeable to oxygen[112] and lead,[113] and has poor adhesion to SiO_2 and other materials used as interlayer dielectrics.[114] Titanium has been used as an adhesion promoting layer for platinum but oxidation of titanium to TiO_2, interdiffusion of platinum and titanium, and hillock formation on the platinum electrode are problems with

the Pt/Ti electrode structure.[115] Therefore, conductive oxides such as IrO_2 and RuO_2 have been introduced to replace the titanium layer in the electrode stack.[113]

Perovskite phased PZT films having good polarization properties and low leakage current can be grown on platinum electrodes.[99,116,117] However, PZT films grown on platinum suffer from poor fatigue resistance.[110,118–120] Oxygen vacancies at the PZT–electrode interface affect the fatigue resistance behavior of PZT.[110,118,120] Better fatigue resistance is obtained when conductive oxides are used as electrode materials but then the films have high leakage currents.[118,120] Good fatigue resistance together with low leakage currents and high remnant polarization have been achieved by using an electrode consisting of about 10 nm thick platinum film grown on conductive oxide such as RuO_2 or IrO_2.[113,116–119] The oxide layer under the thin platinum film is essential in obtaining good fatigue properties because it acts as a sink for oxygen vacancies.[118]

Iridium has been shown to be a suitable electrode material for PZT because high remnant polarization, low leakage currents, and good fatigue properties have been obtained for PZT grown on iridium.[121–123] The good fatigue properties of the PZT films are most probably due to oxidation of the iridium surface during the PZT deposition at temperatures higher than 530 °C.[122] In addition, the IrO_x layer formed on the surface of the iridium electrode prevents diffusion of lead and oxygen through the electrode.[113] Iridium can also be used as an oxygen barrier layer in multilayer electrode structures.[122]

Ruthenium is another electrode material studied for FRAM capacitors with PZT as the ferroelectric.[120] PZT films grown on ruthenium electrodes have better fatigue properties than PZT films grown on platinum electrodes,[120,124] and show higher remnant polarization than PZT films grown on RuO_2.[120] The leakage currents are lower than for PTZ grown on RuO_2 but higher than for PZT grown on platinum.[120] The ferroelectric film cannot be grown on ruthenium electrode at high temperatures because interface reactions take place. PLZT, for example, has been reported to react with ruthenium at temperatures higher than 600 °C.[121,125] Ruthenium can be used as an oxygen diffusion barrier and as an adhesion promoting layer in multilayer electrode structures.[126,127]

2.2.2 Electrodes for $SrBi_2Ta_2O_9$

SBT has better fatigue resistance than PZT, but has low remnant polarization[101] and requires high processing temperatures of 650–700 °C.[101,128] Platinum and iridium have been studied as electrode materials for both FRAM capacitors and FRAM transistors having SBT as the ferroelectric.

Platinum is a widely used electrode material for FRAM capacitors having SBT as the ferroelectric material.[128,129] Electrode stack having the structure of Pt/IrO_2/Ir/Ti(Al)N/W-plug has been proposed for SBT.[128] In this structure, platinum is used as the topmost layer because it forms a stable interface with SBT. IrO_2 is needed as an oxygen diffusion barrier, because platinum is highly permeable to oxygen,[128] as well as to bismuth from the SBT layer.[129] The IrO_2 layer cannot be grown directly on the Ti(Al)N barrier because Ti(Al)N would oxidize during the IrO_2 deposition. Therefore, an iridium layer is needed between IrO_2 and the Ti(Al)N. Ti(Al)N works as a barrier and an adhesion promoting layer, and forms a stable interface with the tungsten plug.[128] However, because of stresses in the electrode stack, hillocks may form on the platinum electrode during high-temperature annealing.[128] Platinum has been used as an electrode material also in MFIS transistors with SBT as the ferroelectric.[108,130]

Iridium is a potential electrode material both in ferroelectric capacitors and in ferroelectric transistors having SBT as the ferroelectric.[108,131] In ferroelectric capacitors, SBT films grown on iridium electrode have been reported to show poor ferroelectric properties, possibly because of oxidation of the iridium surface during SBT processing.[128,131] However, iridium and IrO_2 can be used as oxygen barrier layers together with platinum electrodes in multilayer electrode structures.[128,132] Platinum cannot be grown directly on iridium, because platinum and metallic iridium interdiffuse at temperatures higher than 650 °C.[132] Iridium, on the other hand, cannot be grown directly on the poly-Si plug because it forms iridium silicide.[132] In MFMIS transistors, iridium has been used as the lower metal electrode on which the ferroelectric SBT layer is grown.[108] However, bismuth was reported to diffuse into the iridium electrode during high temperature annealing.[108]

2.2.3 Electrodes for $(Bi,La)_4Ti_3O_{12}$

BLT has good fatigue resistance and large remnant polarization and is therefore a candidate ferroelectric material for FRAMs.[107] Processing temperatures of 650 °C or higher are usually required in preparation of BLT.[107] Platinum has been used as electrode material both in FRAM capacitors[107,133] and in FRAM transistors[109] having BLT as the ferroelectric. In ferroelectric capacitors, however, bismuth readily diffuses into the platinum electrode.[133] Ruthenium is another electrode material studied for BLT.[134] However, higher leakage currents have been measured for BLT grown on ruthenium than for BLT grown on platinum. The surface of the ruthenium electrode becomes oxidized to ruthenium oxide during annealing of the capacitor in oxygen.[134] In multilayer electrode stacks, iridium has also been used as an electrode material.[135]

2.3 Gate electrodes in metal-oxide-semiconductor field effect transistors

In MOSFETs, SiO_2 has been traditionally used as the gate dielectric, and poly-Si as the gate electrode. In order to maintain the capacitance density at the desired level as the transistor dimensions are scaled down, SiO_2 needs to be replaced by a high-*k* dielectric. The high-*k* dielectrics that have been studied as potential alternatives for SiO_2 include for example Ta_2O_5, Al_2O_3, ZrO_2, and HfO_2.[136] The poly-Si gate electrode suffers from depletion effect which decreases the total capacitance of the gate stack. Additional disadvantages of poly-Si are its high electrical resistance and diffusion of boron from the doped poly-Si gate to silicon.[137] Furthermore, most of the high-*k* gate dielectrics are unstable in contact with silicon.[136,138] Therefore, metal gate electrodes are needed to replace the poly-Si gate electrode in the future complementary metal-oxide-semiconductor (CMOS) devices. Figure 4 shows a schematic of a FET with a metal gate electrode.

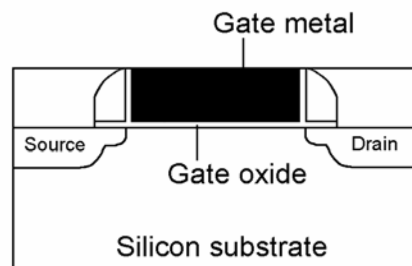

Figure 4. A schematic of field effect transistor with a metal gate electrode.

Noble metals are potential gate electrode materials because they have high work functions. High work function is needed because the threshold voltage of the transistor depends on the work function difference between the gate electrode and the semiconductor. The work function of the poly-Si gate can be easily adjusted by doping, but when a metal gate is used, adjusting of the work function is more complicated. The desired work functions are 5.0–5.2 eV for *p* type MOSFETs, and 4.1–4.3 eV for *n* type MOSFETs.[137] Noble metals have vacuum work functions in the range of 4.7–5.9 eV (Table 1), and are therefore potential gate electrode materials for the *p* type transistors. Alloying of noble metals with a non-noble metal such as tantalum can produce alloys with a work function suitable for the *n* type transistors.[139,140]

The work function of the gate metal depends on the nature of the interface between the gate metal and the gate dielectric. Thus, different work functions are obtained on different gate dielectric materials. The nature of the metal–dielectric interface, and thus the work function of the gate metal, may change for example during post-annealing of the structure.[137,141] The following effective work functions have been reported for noble metals grown on high-*k* dielectrics and SiO_2. For iridium, work functions of 4.5–4.7 eV[137,142] have been reported on HfO_2 and 4.9 eV on SiO_2.[143] For platinum, work functions of 4.6–5.3 eV have been reported on HfO_2,[141,142,144] and for ruthenium, work functions of 4.6–5.3 eV have been reported on HfO_2,[142,145,146] 5.0 eV on Al_2O_3,[146] and 5.1–5.3 eV on SiO_2.[143,146] The effective work functions measured for iridium and platinum are lower than the vacuum work functions given in Table 1 for clean iridium and platinum surfaces.[20] For ruthenium, both higher and lower work functions than the vacuum work function of 4.7 eV[20] have been reported.

The gate electrode should be chemically stable with the gate dielectric during the electrode deposition process and the high-temperature post-annealings needed for the device fabrication. Studies on the stability of the iridium–Ta_2O_5[147] and iridium–HfO_2[137] interfaces show that the structures are unstable during high-temperature annealing; metallic tantalum forms at the iridium–Ta_2O_5 interface during annealing at 750 °C,[147] and significant interdiffusion takes place at the iridium–HfO_2 interface at 800 °C.[137] Integration of iridium gate electrode in the SiO_2 based MOSFETs has also been studied; the iridium–SiO_2 interface was found to be stable during annealing up to 900 °C.[148] The platinum–HfO_2[141,149] and platinum–ZrO_2[150] interfaces have been reported to be stable up to 500 and 600 °C, respectively. However, platinum has poor adhesion to most of the dielectric materials.[136,151] Palladium has not been extensively studied as the gate electrode although

the palladium–HfO_2 interface was reported to be stable up to 500 °C.[149] Ruthenium films grown by sputtering have been reported to be stable in contact with ZrO_2 and SiO_2 even during annealing at 800 °C.[152] When the ruthenium films were grown by digital CVD, a thin amorphous ruthenium oxide layer was reported to form at the ruthenium–HfO_2 interface.[145] However, since ruthenium oxide is conductive, this layer does not decrease the total capacitance of the gate stack. The conductive oxides RuO_2 and IrO_2 are potential gate electrode materials as well.[136,153]

Ruthenium seems to be the most suitable noble metal electrode material because no detrimental interface reactions or interdiffusion take place at the ruthenium–dielectric interface. Furthermore, work function values suitable for *p* type transistors have been reported for ruthenium electrodes. In addition, etching of ruthenium is easy.[54] Platinum electrodes, on the other hand, are difficult to etch and suffer from poor adhesion to the dielectrics. Iridium is another potential gate electrode material. However, poor stability of the iridium–dielectric interface at high temperatures may be a problem.

ALD has been shown to be a suitable method for deposition of high-*k* gate dielectrics to MOSFETs.[136] Thus, ALD could be used for deposition of the gate electrodes as well. The gate electrode is grown on the gate dielectric, and therefore, oxidizing noble metal processes can be used for growing the gate electrode. However, oxidation of the underlying silicon gate during gate electrode deposition may be a concern.[146] Ruthenium, platinum, and iridium films grown by the ALD processes presented in Papers I, II, and V have already been studied as gate electrodes.[142]

2.4 Copper seed layers and barriers in interconnect metallization

Copper is replacing aluminum as the interconnect material in ICs because of its low resistivity and high electromigration resistance. Diffusion of copper to the interlayer dielectric must be prevented by using a barrier layer between copper and the dielectric. Transition metal nitrides are widely used as barrier materials, but they require an additional seed layer, conventionally a thin copper layer, for subsequent copper electroplating.[154] However, deposition of conformal copper seed layers with high enough quality is difficult.[155,156]

The use of noble metals as seed layers for copper electroplating, and possibly also as copper diffusion barrier layers, has recently gained interest. Ruthenium, palladium,

rhodium, iridium, platinum, and silver have low enthalpies for oxide formation, and therefore, direct electroplating of copper on their surface is possible in acidic electrolyte without oxidation of the noble metal surface.[157] Thus, no additional copper seed layer is needed for copper electroplating. Direct electroplating of copper has been reported on ruthenium,[154,155,157] iridium,[158] palladium,[157] and rhodium.[157] If the noble metal layer is able to prevent copper diffusion to the interlayer dielectric, no additional diffusion barrier layer is needed, and the noble metal works as a combined barrier and seed layer. If the noble metal layer does not have sufficient barrier properties, an additional copper diffusion barrier layer is still needed.

Ruthenium is a potential material as a combined barrier and seed layer because it has low solid solubility in copper up to 900 °C.[154] No new phases were detected at the ruthenium–copper interface after annealing at 800 °C indicating stability of the interface.[154] A 20-nm thick ruthenium film deposited by sputtering has been reported to prevent copper diffusion up to 450 °C during annealing in vacuum.[159] However, copper diffusion along the grain boundaries of crystalline ruthenium films may still turn out to be a problem. Ruthenium works also as an adhesion promoting layer since adhesion between copper and ruthenium is strong.[154,156,157,159] Both (111) oriented[154] and non-oriented[157] copper films have been obtained by electroplating on ruthenium surface; (111) is a more desirable crystal orientation for copper because of its lower susceptibility to electromigration.[154]

Iridium is another potential material for copper seed layer. Figure 5 shows a trench with an iridium seed layer grown by the ALD process presented in Paper V. Copper was directly electroplated on the iridium seed layer, and the trench was filled with copper without formation of any voids.[158]

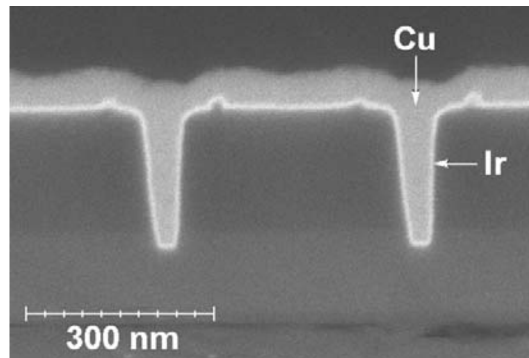

Figure 5. A trench with an iridium seed layer grown by ALD. Copper was electroplated directly on the iridium seed layer.[158]

Palladium does not have good barrier properties because it diffuses in copper already at 400 °C but it can be used as a seed layer for both electroplating and electroless plating of copper.[157,160,161] Both (111) oriented[160] and non-oriented[157] electroplated copper films have been obtained on palladium.

The copper interconnects are fabricated by using dual-damascene processing. Figure 6 shows an example of a dual-damascene interconnect structure. In dual-damascene processing, the barrier and seed layers should have nearly perfect step coverage, uniform thickness over the substrate, and they should be grown at temperatures lower than 400 °C.[162] In addition, the barrier and the seed layers should have low resistivities and low halide contents, be CMP compatible, and have good adhesion to all materials they are in contact with.[162] Thus, both the barrier and the seed layers need to fulfill strict demands. The maximum thickness of the single barrier layer or the barrier stack is restricted by the dimensions of the interconnects. In 2003, the via diameter was 90 nm but it will eventually decrease down to 45 nm.[163] In the future devices, the acceptable total thickness of the barrier and the seed layers will be less than 7 nm.[154,159]

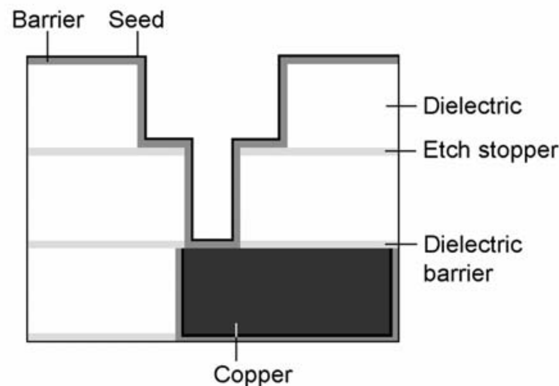

Figure 6. An example of a dual-damascene interconnect structure. In the next processing step copper is electroplated on the seed layer.

ALD is a suitable method for barrier and seed layer deposition into the dual-damascene structures because of the excellent conformality of the films grown by ALD.[11,156,158] ALD of transition metal nitride diffusion barriers,[12] and copper seed layers[15] have been widely studied, and ALD is considered a potential method for noble metal seed and barrier layer deposition as well.[155,158,164] If an additional nitride barrier is used, the noble metal seed probably needs to be grown in reducing conditions in order to avoid oxidation of the barrier. If, on the other hand, no additional barrier is used but the noble metal layer is grown directly on the interlayer dielectric, oxidizing process conditions may also be used.

3. EXPERIMENTAL METHODS

3.1 Film growth

The films were grown in a flow-type hot-wall F120 ALD reactor[3] (ASM Microchemistry, Finland) and the *in situ* experiments were carried out in a specially modified F120 ALD reactor.[165] The reactor pressures were 10 mbar and 2 mbar, respectively. Solid precursors were vaporized from glass crucibles held inside the reactor, while gaseous precursors were introduced into the reactor from external reservoirs. The flow rate of the gaseous precursor was adjusted with a needle valve and measured with a mass flow meter. Pulsing of the precursors was accomplished by solenoid valves. The noble metal precursors studied in this work as well as the process conditions used are summarized in Paper VIII. Depending on the process, either air or oxygen (99.999 %) was used as the other reactant, and nitrogen (99,999 %) or argon (99.99 %) as both purging and carrier gas. In most of the film growth experiments, the substrate was coated with a thin Al_2O_3 film just prior to noble metal deposition. The Al_2O_3 film was grown from $AlCl_3$ and water[166] and its function was to provide uniform hydroxyl group coverage on the surface, and thus facilitate uniform nucleation of the noble metal film. The substrate size was 5 cm x 5 cm.

In the *in situ* reaction mechanism studies, the gas phase species were analyzed with a Hiden HAL/3F 501 RC quadrupole mass spectrometer (QMS) using a Faraday cup detector and ionization energy of 70 eV. Sampling and pressure reduction from 2 mbar to about 10^{-4} mbar were accomplished by differential pumping through a 200 μm orifice. Mass changes were analyzed with a Maxtek TM-400 quartz crystal microbalance (QCM).

3.2 Film characterization

The films grown were analyzed with various methods. The crystalline phases were identified by X-ray diffraction (XRD) and the film thickness and the surface roughness were determined by X-ray reflectivity (XRR). Energy dispersive X-ray spectroscopy (EDX, EDS) was the principal method used for the film thickness determination. The surface morphology of the films was studied by scanning electron microscopy (SEM) and atomic force microscopy (AFM). Time-of-flight elastic recoil detection analysis (TOF-ERDA) was performed to analyze the impurity contents of the films. Electrical resistivities

of the metal films were calculated from the sheet resistances measured by a four-point-probe. The analysis techniques used in this work are described in the following.

3.2.1 X-ray diffraction and X-ray reflectivity

XRD was used to detect the crystalline phases present in the film. The measurements were made by using a θ–2θ scan mode, where θ is the angle between the incident beam and the substrate surface. With this measurement setup, only crystal planes parallel to the substrate are detected. Preferred crystal orientations in the films were determined by comparing the relative intensities of the detected peaks to the reference values for randomly oriented powder samples.[21] Rocking curve measurements were performed in order to get further information of the orientation of the grains. In the rocking curve measurement, the X-ray tube and detector were held at a specific Bragg angle 2θ, and were rotated in respect to the substrate. The width of the obtained peak tells how well the grains are oriented; the wider the peak, the broader the distribution in the grain orientation.

XRR can be used for determining the thickness, roughness, and density of the films. In XRR, the X-ray beam is directed to the material at grazing angles of incidence (0.0–3.0°), and the intensity of the specular reflection is measured. Examples of XRR reflectivity curves are shown in Figure 12 on page 44 and in Paper V. The incident X-ray beam undergoes total reflection from the film surface at incident angles lower than the critical angle for reflection. At angles higher than the critical angle, the incident beam penetrates into the film, and the intensity of the reflected X-rays decreases significantly. The density of the material can be determined on the basis of the value of the critical angle.[19,167,168] The accurate determination of the density requires accurate calibration of the angle between the incident beam and the surface. Due to difficulties in calibrating the tool in high enough accuracy, the density values are not presented in the results.

Above the critical angle, the incident beam penetrates into the film and reflects from all interfaces at which the electron density, and thus the refractive index of the material, changes. Interference between X-rays reflected from the film surface and film–substrate interface are responsible for formation of the oscillatory pattern, also called Kiessig fringes, in the reflectivity curve. The film thickness can be determined from the distance of the oscillations.[19,167,168] The film thickness range analyzable by XRR depends greatly on the sample. In the present study, film thicknesses in the range of 10–100 nm could be determined by XRR. The advantage of XRR in the film thickness determination is that it is

an absolute measurement which directly gives the thickness without the need to know other film properties, such as the density of the material. In addition, no reference samples or standards are needed, either.

Increasing surface roughness of the films leads to a decrease in the intensity of the reflected beam. The surface roughness of the film can thus be determined from the decrease of the signal intensity in the reflectivity curve.[167,168] For very rough surfaces, the intensity decrease smears out the oscillation pattern and the thickness determination becomes impossible. XRR can be used for detecting short scale roughness of the surface. However, large scale inhomogeneities are averaged out in the XRR analysis.

A Bruker AXS D8 Advance XRD instrument using copper Kα X-ray beam was used in both the XRD and the XRR analysis. A Göbel mirror was used for generating parallel beam geometry.

3.2.2 Scanning electron microscopy and energy dispersive X-ray spectroscopy

SEM images were taken to study the surface morphology and the conformality of the films. Both secondary electrons released by the primary electron beam and electrons backscattered from the surface were used for imaging. Topography differences are more clearly visualized by the secondary electrons while backscattered electrons provide better material contrast.

Electrons are removed from the inner shells of the sample atoms by the electron bombardment, and X-rays are produced when the atoms relax to the ground state after ionization. With EDX, both qualitative and quantitative analysis can be made on the basis of the emitted X-rays.[169] Since elements with atomic number below 11 could not be quantitatively analyzed with the tool used, the hydrogen, carbon, and oxygen impurities could not be analyzed by EDX. Thus, EDX was used only for determining the film thicknesses.

The EDX analyses were made with a Link ISIS spectrometer attached to a Zeiss DSM 962 SEM. The acceleration voltage used in the EDX measurements was 20 keV. Figure 7 shows the EDX energy spectra obtained from ruthenium, iridium, and platinum films. The analysis of ruthenium films was done by using the Lα peak at 2.6 keV. For, iridium the Lα peak at 9.2 keV gave more reliable thickness values than the Mα peak at 2.0 keV because

the Mα peak overlaps with the silicon Kα peak at 1.7 keV (Figure 7a). For the same reason, the Lα peak at 9.4 keV instead of Mα at 2.1 keV was used for analysis of platinum (Figure 7b). The analysis of the palladium films was made by using the Lα peak at 2.8 keV and the analysis of the rhodium films by using the Lα peak at 2.7 keV.[170]

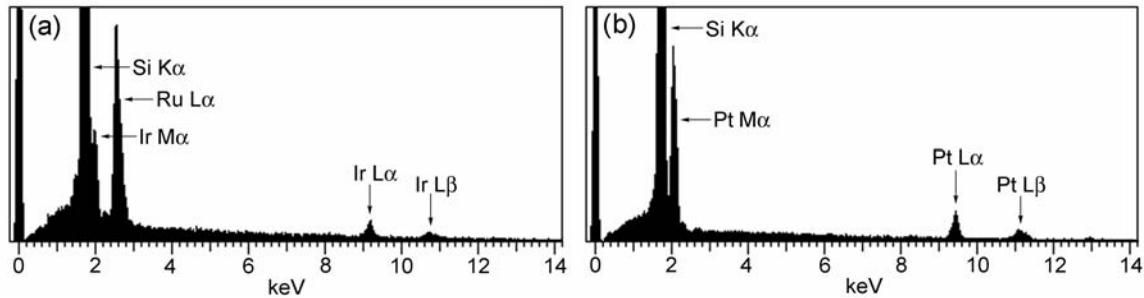

Figure 7. EDX energy spectra measured from (a) ruthenium (70 nm)/iridium (20 nm)/Al_2O_3/Si and (b) platinum (50 nm)/Al_2O_3/Si film structures. The peaks for aluminum and oxygen are not clearly distinguishable. The thicknesses given in the parenthesis are obtained from the analysis of the spectra.

The intensity ratio $k = I / I_{standard}$ for each element was calculated by using theoretical standards and the film thicknesses were calculated from the k values using a GMR electron probe thin film microanalysis program.[171] Bulk densities of the noble metals (Table 1) were used in the thickness calculation, which probably caused some error in the obtained thickness values since the films were likely to have densities lower than the bulk density. Therefore, the film thickness values obtained from EDX analysis are likely to be smaller than the actual film thicknesses.

3.2.3 Atomic force microscopy

The surface morphology and surface roughness of the noble metal thin films were studied by AFM, which was operated in the intermittent-contact mode, also called the tapping mode. In the intermittent-contact mode AFM, the film surface is probed with a sharp tip that is attached to a cantilever. The system vibrates the cantilever near its resonance frequency that depends on the distance between the tip and the sample surface. Changes in the frequency are then used for imaging the surface topography. The tip vibrates very close to the surface just barely hitting the surface so that no lateral forces are applied to the surface. The intermittent-contact mode is suited for imaging large areas that include variation in the sample topography. The AFM analyses were made with an AutoProbe CP AFM (Park Scientific Instruments/Veeco).

3.2.4 Time-of-flight elastic recoil detection analysis

The impurity contents of the noble metal films were analyzed by TOF-ERDA[172,173] which is a suitable method for analyzing light elements in a heavy matrix. The analyses were performed with an EGP-10-II tandem accelerator.[172] In TOF-ERDA, the sample is bombarded by an ion beam, and the recoiled sample atoms released from the sample in elastic collisions are analyzed. The probability for elastic scattering increases with increasing atomic number, mass, and the energy of the primary ion. Therefore, heavy primary ions with masses of 79–127 *u* and energies of 48–58 MeV were used in the analysis of the noble metal samples. The time-of-flight and the energy of the recoil atoms are analyzed by separate time-of-flight and energy detectors. The mass of each detected atom can then be calculated from the classical formula for kinetic energy, and the atoms can thus be identified. Figure 8 shows TOF-ERDA data collected from a 145-nm rhodium film on silicon.[VII] The recoil atoms and the primary ion have been identified on the basis of the time-of-flight *vs*. energy data.

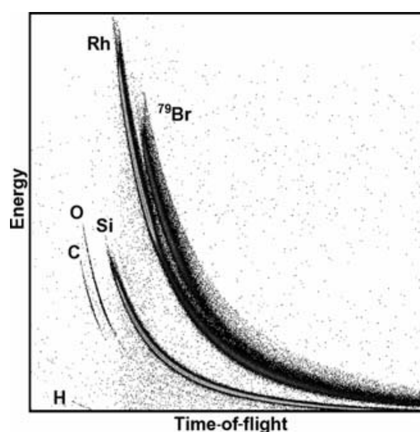

Figure 8. Time-of-flight *vs*. energy data measured from a 145-nm thick rhodium film on silicon by using 40 MeV $^{79}Br^{8+}$ ions as the primary beam.[VII] The contour curves denote the intensity of the signals. Analysis of the data reveals that the film contains less than 0.1 at.% H, 1.6 at.% C, and 2.3 at.% O.[VII]

The atomic concentration of the different elements in the sample can be calculated from the number of the detected recoil atoms by using the probability function for a sample atom to recoil to a specific detector angle. The recoil atoms lose energy as they move through the sample, and thus, the energy of the detected atoms decreases with increasing original distance from the sample surface. Thus, depth profiles of the elements can be obtained from their energy distribution, and atoms originating from the film can be separated from the atoms originating from the substrate.[172,173]

3.2.5 Electrical measurements

Electrical resistivities of the noble metal films were calculated from sheet resistances measured by a four-point-probe. The four-point-probe has four equally spaced probes that are pushed against the substrate. A constant current is applied between the outer probes and the voltage difference is measured between the inner probes. The probes are relatively sharp to minimize the contact area between the probe and the film. When measuring resistances of very thin or soft films, the probes may penetrate through the film making the measurement unreliable. The film resistivities were calculated from the measured sheet resistances by multiplying them with the film thicknesses obtained by EDX or XRR. The measurements were performed with a Keithley 2400-SourceMeter and Alessi C4S four-point-probe head.

The bulk resistivities of noble metals are in the range of 1.5–9.8 $\mu\Omega\cdot$cm (Table 1). Thin films usually have resistivities higher than the bulk resistivity because of the effect of impurities, grain boundaries, surface roughness, and in very thin films also surface scattering.[163,174] Since the film thickness is needed in calculation of the resistivities, error in the film thickness also causes error in the calculated resistivity values; if the measured film thickness is smaller than the actual value, as can be the case in thicknesses determined by EDX, too low resistivities are obtained.

4. ALD OF NOBLE METALS

Noble metal ALD processes have been reported for ruthenium,[I,IV,37,156,175,176] platinum,[II,39] iridium,[V,38] palladium,[37,177] and rhodium.[VII,178] So far, no ALD processes have been reported for gold, silver, and osmium. The difficulty with ALD of silver and gold is the poor thermal stability of many organometallic silver and gold compounds.[179,180] There are some reports on CVD of osmium from organometallic osmium precursors,[181] but the suitability of these precursors for ALD has not been reported.

Many of the reported noble metal ALD processes are based on similar type of chemistry as the noble metal CVD processes, which have been widely studied.[182–185] Despite the same precursor combinations used in ALD and CVD, the reaction mechanisms in the ALD processes are likely to differ from those in the CVD processes because in ALD the precursors are led into the reaction chamber in alternate pulses. In addition, stability of the precursors against thermal self-decomposition is a critical factor in ALD. There is still a large amount of volatile noble metal compounds that have not been studied in ALD.[180,186] The number of oxidants and reducing agents studied in ALD processes is very limited as well. Therefore, it is likely that the process window for ALD of noble metals can be further expanded by using new precursor combinations. The following sections contain a review of the so far reported noble metal ALD processes and their reaction mechanisms. The processes studied in the present work are also reviewed in Paper VIII.

4.1 Film growth

4.1.1 Ruthenium

ALD of ruthenium has been reported from cyclopentadienyl compounds $RuCp_2$[I,VI] (Cp = cyclopentadienyl) and $Ru(EtCp)_2$ (Et = ethyl),[156,175] and from β-diketonate compounds $Ru(od)_3$ (od = 2,4-octanedionato)[176] and $Ru(thd)_3$ (thd = 2,2,6,6-tetramethyl-3,5-heptanedionato).[IV,37] The mechanisms of these processes are based either on oxidation of the ruthenium precursor by oxygen,[I,IV,156,176] or on reduction by NH_3 plasma[175] or hydrogen.[37] In patent literature, the use of hydrazine (H_2NNH_2) and its derivatives as reducing agents in ALD of ruthenium has also been mentioned.[187] The reported ruthenium ALD processes are summarized in Table 2.

Table 2. Summary of the reported ruthenium ALD processes.

Metal precursor	$T_{vaporization}$ (°C)	Reaction gas	Flow rate (sccm)	T_{growth} (°C)	Ref.
$RuCp_2$	45–70	Air	2–8	275–400	**I**
	60	O_2	5	225–275	**VI**
$Ru(EtCp)_2$	80	O_2	20–120	270	156
	80	NH_3 plasma	100	270	175
$Ru(od)_3$	200	O_2	100	275–450	176
$Ru(thd)_3$	100	Air	40	325–450	**IV**
	100	O_2	20	250–325	**VI**
	180	H_2	separate reduction step	180/300	37

$RuCp_2$[I,VI]

ALD of ruthenium from $RuCp_2$ and O_2 has been reported in Papers I and VI. $RuCp_2$ has melting point of 195 °C,[188] but its vapor pressure is relatively high also in the solid state.[182] $RuCp_2$ is stable during short exposures to air which makes it easy to handle. Both pure oxygen[VI] and air[I] have been used as oxygen sources. Ruthenium films could be grown on Al_2O_3 at temperatures of 275–400 °C,[I] whereas on iridium or platinum seed layer, the film growth took place already at 225 °C.[VI] The film growth rate varied from about 0.10 Å/cycle at 225 °C[VI] to about 0.55 Å/cycle at 400 °C.[I] At 350 °C, the growth rate saturated to about 0.45 Å/cycle with $RuCp_2$ and air pulse times longer than 0.5 and 1.0 s,

respectively. Constant growth rates were measured also when the $RuCp_2$ dose was varied by varying its sublimation temperature between 50–70 °C.[I] At air flow rates of 8 standard cubic centimeters per minute (sccm) or higher, the film growth rate and the surface roughness increased; the films lost their mirror-like appearance and became milky-like.[I] Figure 9 shows an AFM image of a 85-nm thick ruthenium film grown at 350 °C from $RuCp_2$ and air. The air flow rate was 4 sccm. The film has root mean square (rms) surface roughness of about 5 nm.

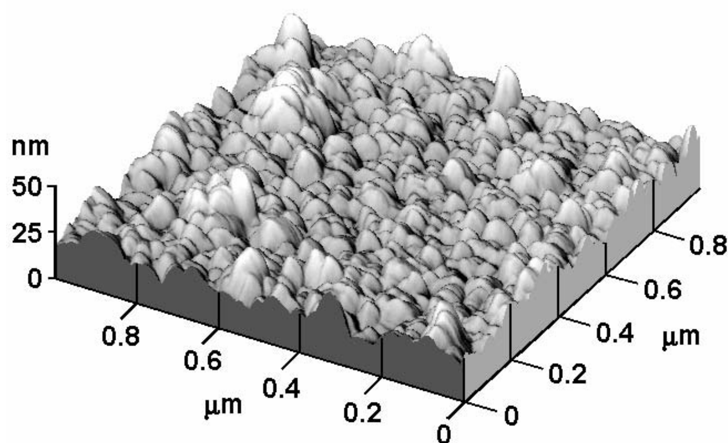

Figure 9. AFM image of a 85-nm ruthenium film grown at 350 °C from $RuCp_2$ and air.

All the films grown from $RuCp_2$ and air were metallic ruthenium as analyzed by XRD.[I] The SEM image in Figure 10 shows the excellent conformality of a ruthenium film grown at 350 °C. It is also visible in the SEM image that the film has a columnar grain structure. Transmission electron microscopy (TEM) studies on ruthenium films grown from $RuCp_2$ and air at 350 °C have also shown the columnar grain structure of the films.[189] The films grown at 300 °C were randomly oriented while the films grown at higher temperatures had a preferred (002) orientation.[I] The resistivities of the ruthenium films increased with decreasing film thickness; a 160-nm film grown at 350 °C had a resistivity of 12 $\mu\Omega\cdot$cm while a 40-nm film grown at the same temperature had a resistivity of 18 $\mu\Omega\cdot$cm.[VIII] The thickness of the ruthenium films grown at 350 °C increased linearly with the number of growth cycles, thus enabling easy and accurate control of the film thickness. At 300 °C, there was a relatively long incubation time for onset of the film growth but after that, linear dependence between the film thickness and the number of the growth cycles was obtained.[I]

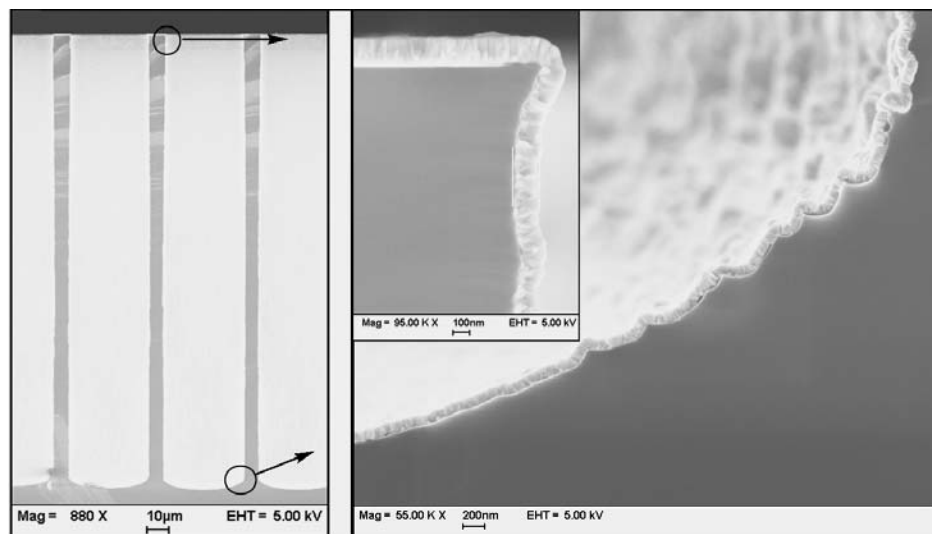

Figure 10. Trenches covered by a ruthenium film grown from $RuCp_2$ and oxygen. Magnifications of the upper and lower corners of the trench are shown on the right.

The ruthenium films grown from $RuCp_2$ and air at 350 and 400 °C had only traces of impurities; on the basis of the TOF-ERD analysis, the films contained less than 0.5 at.% hydrogen, carbon, and oxygen, each. In the films grown at 300 °C, the oxygen content was higher but still less than 1.5 at.%.[**I**] The ruthenium films grown on Al_2O_3 were uniform and had good adhesion. On the contrary, films grown directly on borosilicate glass or silicon with native oxide were non-uniform and of poor quality. It is likely that a uniform coverage of hydroxyl groups on the as-deposited Al_2O_3 surface promotes uniform nucleation of the ruthenium films.[**I**]

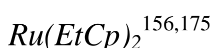

$Ru(EtCp)_2$[156,175]

Ruthenium thin films have been grown from $Ru(EtCp)_2$ at temperature of 270 °C by conventional, thermally activated ALD[156] and by plasma enhanced ALD (PEALD).[175] Studies on CVD of ruthenium from $Ru(EtCp)_2$ have shown that $Ru(EtCp)_2$ is thermally stable in vacuum up to 400 °C and that it reacts with oxygen already at temperatures above 220 °C.[190] Hence, because of its thermal stability and reactivity with oxygen, $Ru(EtCp)_2$ can be expected to be a suitable precursor for ALD as well. Furthermore, $Ru(EtCp)_2$ is a liquid at room temperature, which simplifies its use as an ALD precursor. $Ru(EtCp)_2$ vaporization temperature of 80 °C was used in the reported ALD processes.[156,175] Films grown by thermally activated ALD from $Ru(EtCp)_2$ and oxygen had resistivities of 15 $\mu\Omega\cdot$cm and contained less than 2 at.% carbon and oxygen. Adhesion of the films to TiN was good.[156] The films grown by PEALD from $Ru(EtCp)_2$ and NH_3 plasma had slightly

lower resistivities of 12 $\mu\Omega\cdot$cm and impurity levels beyond the detection limits of TOF-ERDA.[175] A 50-nm thick ruthenium film grown by PEALD had a rms surface roughness of 0.7 nm whereas a 50-nm film grown by thermally activated ALD had a higher surface roughness of 3.1 nm. The densities of the films grown by thermally activated ALD and PEALD were 8.7 and 12.0 g/cm^3, respectively.[175] The ruthenium films grown by PEALD had a preferred (002) orientation[175] while the films grown by thermally activated ALD had a preferred (101) orientation.[156] The differences between the ruthenium films grown by PEALD and thermally activated ALD were suggested to be due to the effect of energetic plasma species that interact with the surface.

Films grown by thermally activated ALD from $Ru(EtCp)_2$ and oxygen at 270 °C had a growth rate of 1.5 Å/cycle[156] whereas the films grown by PEALD from $Ru(EtCp)_2$ and NH_3 plasma had a growth rate of 0.38 Å/cycle.[175] The growth rate obtained in the thermally activated $Ru(EtCp)_2$ process was also much higher than the growth rates obtained in the oxygen-based $RuCp_2$**I** and $Ru(thd)_3$**IV** ALD processes, which were also thermally activated. The film growth rate in the thermally activated $Ru(EtCp)_2$ process was reported to depend on the oxygen partial pressure during the oxygen pulses; when the oxygen flow rate was decreased from 80 sccm to 20 sccm, the growth rate decreased from 1.5 to 0.65 Å/cycle.[156] This change may be related to the amount of adsorbed oxygen on the ruthenium surface. As the partial pressure of oxygen increases, more oxygen adsorbs on the surface, higher portion of the EtCp ligands are consumed in the reaction with the adsorbed oxygen, and more $Ru(EtCp)_2$ molecules are able to adsorb on the surface. It is also evident that as the amount of adsorbed oxygen increases, longer $Ru(EtCp)_2$ pulse times are needed to remove all the adsorbed oxygen. In fact, it was reported that with short $Ru(EtCp)_2$ pulse times RuO_2 was formed.[156] Thus, it seems that the high growth rate and the RuO_2 formation are due to the high oxygen partial pressure used in the process. The reaction mechanisms of the noble metal ALD processes are discussed in more detail in Chapter 4.2.

$Ru(od)_3$[176]

Ruthenium has been grown by ALD from a β-diketonato compound $Ru(od)_3$ and oxygen.[176] $Ru(od)_3$ is a viscous liquid which at the atmospheric pressure vaporizes at 310 °C.[191] In the ALD experiments, $Ru(od)_3$ was dissolved in 0.1 M *n*-butyl acetate, and the solution was injected into a vaporizer which was kept at 200 °C. The oxygen flow rate was 100 sccm. The films were grown at temperatures between 275 and 450 °C. At growth temperatures between 275 and 375 °C, growth rates of 0.6–0.9 Å/cycle were obtained on

SiO_2/Si wafer.[176] At temperatures higher than 375 °C, the growth rate increased rapidly indicating thermal self-decomposition of Ru(od)$_3$. TEM-EDX analysis of films grown on carbon nanotubes revealed that the films contained detectable amounts of carbon and oxygen.[176] Because the film growth was performed in non-saturative conditions, incomplete surface reactions may be responsible for incorporation of the carbon and oxygen impurities. During annealing in oxygen at 500 °C for one hour, the ruthenium films oxidized to ruthenium oxide.[176]

Ru(thd)$_3$[IV,VI,37]

Another β-diketonato precursor that has been studied for ALD of ruthenium is Ru(thd)$_3$, which has been used both in oxygen-based[IV,VI] and in hydrogen-based processes.[37] Ru(thd)$_3$ has a melting point of 216 °C[188] and is relatively stable against air and moisture. In the reported ALD processes, Ru(thd)$_3$ has been sublimated at temperatures of 100 °C[IV,VI] and 180 °C.[37] In the latter case, ruthenium was grown on high surface area support, and the higher sublimation temperature of 180 °C was needed to obtain high enough Ru(thd)$_3$ dose to saturate the very large surface area.

In the oxygen-based process, both air and pure oxygen have been used as oxygen sources.[IV,VI] The air and oxygen flow rates were 40 and 20 sccm, respectively. On Al_2O_3, films were obtained at growth temperatures of 325 °C and higher. The upper temperature limit for the process was 450 °C because of thermal self-decomposition of Ru(thd)$_3$.[VI] On iridium surface, the film growth took place already at 250 °C.[VI] When air was used as the oxygen source, the growth rate at 350 °C saturated to 0.36 Å/cycle.[IV] With pure oxygen, the growth rate at 250 °C was 0.15 Å/cycle.[VI] Figure 11 shows the XRD pattern of a ruthenium film grown from Ru(thd)$_3$ and oxygen on iridium seed layer at 325 °C. In the XRD pattern shown in Figure 11, the intensity ratio of the ruthenium (002) and (101) reflections is 1.2 : 1 whereas in a randomly oriented powder, the ratio would be 0.35 : 1.[21] Thus, the film grown at 325 °C has a preferred (002) crystal orientation. The fraction of the crystals having the (002) orientation increases with increasing growth temperature; in a XRD pattern of a ruthenium film grown at 450 °C the intensity ratio was 3.2 : 1.[IV] The impurity contents of the films grown from Ru(thd)$_3$ and air at 350 °C were analyzed by TOF-ERDA; the films contained 2.2 ± 0.5 at.% hydrogen, 1.2 ± 0.3 at.% carbon, and 4.1 ± 1.0 at.% oxygen.[IV]

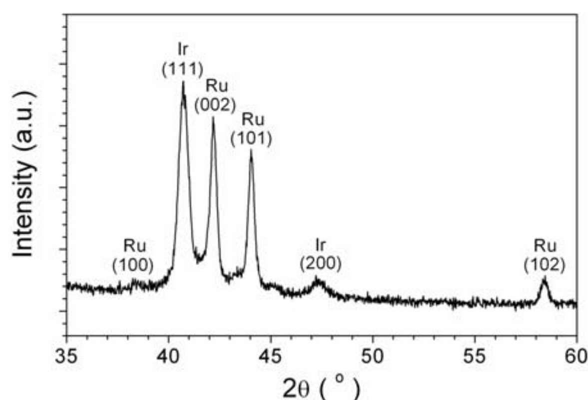

Figure 11. XRD pattern of a ruthenium film grown from $Ru(thd)_3$ and oxygen on iridium seed layer at 325 °C.

Ruthenium has been deposited from $Ru(thd)_3$ on high surface area Al_2O_3 and SiO_2 supports by a hydrogen-based ALD process.[37] $Ru(thd)_3$ was sublimated at 180 °C to ensure sufficient dose of the vaporized precursor to saturate the large surface area. The supports were exposed to $Ru(thd)_3$ at 180 °C, and the adsorbed precursor was then reduced by hydrogen in a separate reducing step at 300 °C. Thus, only one growth cycle was applied in these experiments. A low ruthenium content of 0.1–0.3 ruthenium atoms/nm^2 was obtained on the supports, which was suggested to be due to a low reactivity of $Ru(thd)_3$ with the surface hydroxyl groups, or to a high desorption rate of the precursor at 180 °C.[37]

In the above presented ALD processes for ruthenium, the growth temperature range was 225–450 °C. The onset temperature of the film growth depended on the reactivity of the ruthenium precursor and on the nature of the initial growth surface; films were obtained at lower temperatures from $RuCp_2$ than $Ru(thd)_3$, and film growth took place at lower temperatures on catalytically active iridium surface than on Al_2O_3.[VI] The crystal orientation of the films depended on the ruthenium precursor, on the growth temperature, and on the type of the process (thermally/plasma activated). Ruthenium films with a random orientation, with a preferred (002) orientation, and with a preferred (101) orientation were obtained. The (002) orientation is thermodynamically the most stable one, and the crystals tend to become (002) oriented at high growth temperatures,[I,IV] or when the surface atoms obtain energy from a high energy plasma.[175]

The growth rates obtained in the ruthenium ALD processes varied from 0.1 to 1.5 Å/cycle. Low growth rates were obtained at low growth temperatures and at low oxygen partial pressures. Ruthenium films with very low impurity contents can be grown by ALD; films

having less than 0.4 at.% hydrogen, carbon, and oxygen were obtained with an oxygen-based process.[I] Only when high oxygen partial pressures were used, a significant amount of oxygen was left into the films.[156] The resistivities of the ruthenium films, when reported, were in the range of 12–20 $\mu\Omega$·cm depending on the film thickness and the precursors used. These values are slightly higher than the ruthenium bulk value of 7.1 $\mu\Omega$·cm.[20]

4.1.2 Platinum

ALD of platinum thin films has been studied from two different platinum precursors: $MeCpPtMe_3$ (Me = methyl)[II,VI,39] and $Pt(acac)_2$ (acac = acetylacetonato).[VIII,192] Table 3 summarizes these platinum ALD processes.

Table 3. Summary of the reported platinum ALD processes.

Metal precursor	$T_{vaporization}$ (°C)	Reaction gas	Flow rate (sccm)	T_{growth} (°C)	Ref.
$MeCpPtMe_3$	RT	Air	40	300	**II**
	RT	O_2	20	200–300	**VI**
	70	Air	separate calcination and reduction steps	100/350	39
		Air, H_2		100/350/300	
$Pt(acac)_2$	155	H_2	30	250	192
	120	O_2	20	210–220	**VIII**

$MeCpPtMe_3$[II,VI,39]

Platinum thin films have been grown by ALD from $MeCpPtMe_3$ and oxygen.[II,VI] $MeCpPtMe_3$ was vaporized at room temperature, which is slightly below its melting point of 30 °C.[193] The vapor pressure of $MeCpPtMe_3$ at room temperature is relatively high.[193] $MeCpPtMe_3$ is air-sensitive, and must therefore be handled under an inert gas. Air with flow rate of 40 sccm[II] or pure oxygen with flow rate of 20 sccm[VI] was used as the other reactant. When pure oxygen was used as the reactant, platinum films were obtained at temperatures of 200–300 °C.[VI] When air was used as the oxygen source, films were obtained only at temperatures of 300 °C and higher.[II] Thermal self-decomposition of $MeCpPtMe_3$ becomes significant above 300 °C, which is therefore considered the upper temperature limit for this process.[II] The results thus show that at temperatures lower than 300 °C the reactivity of the precursors increases with increasing oxygen partial pressure.

The impurity contents of the films grown with air at 300 °C decreased with increasing air pulse time; the films contained less than 0.5 at. % hydrogen, less than 0.5 at. % carbon, and less than 1.0 at. % oxygen when long air pulse times of 2.0 s were used.[II] If pure oxygen is used as reactant, shorter pulse times are likely to be needed to complete the surface reactions. The films grown at 200 °C with pure oxygen contained less than 0.5 at.% of hydrogen, carbon, and oxygen, each.[VI] Thus low impurity contents were also obtained at low growth temperatures.

The growth rates of the platinum films grown at 300 °C from $MeCpPtMe_3$ were about 0.5 Å/cycle both when air and pure oxygen were used as oxygen sources.[II,VI] At 200 °C, the growth rate was 0.30 Å/cycle. The thickness of the platinum films grown at 300 °C using air depended linearly on the number of the growth cycles at the studied thickness range of 35–110 nm.[II] The films grown at 300 °C using air had relatively rough surfaces; AFM analysis showed that a 50-nm platinum film had a surface roughness of about 4 nm.[I] The films grown using pure oxygen had smoother surfaces since a 50-nm platinum film grown at 300 °C had a surface roughness of 1.2 nm as analyzed by AFM.[VI] Figure 12 shows an XRR pattern measured from a platinum film grown at 250 °C with pure oxygen. The roughness value obtained from simulation of the curve was 1.2 nm which is comparable to the roughness value of 0.8 nm obtained by AFM analysis for the same film.[VI] The resistivities of the platinum films were low; a 30-nm film grown at 200 °C had a resistivity of 17 $\mu\Omega\cdot$cm and a 50-nm film grown at 300 °C had a resistivity of 13 $\mu\Omega\cdot$cm.[VI] Adhesion of the films to Al_2O_3 was moderate; the films grown with air as the oxygen source did no pass the tape test,[II] while the films grown with pure oxygen passed the tape test.[VI]

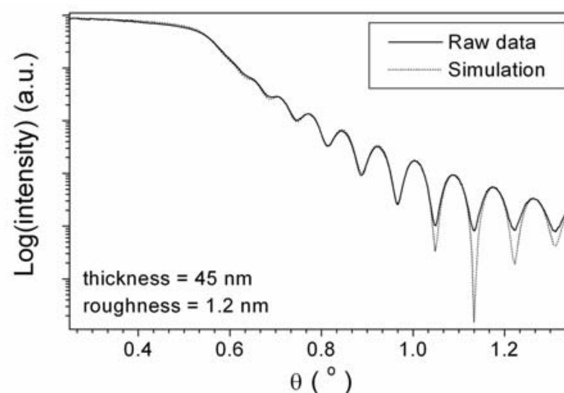

Figure 12. XRR pattern of a platinum film grown at 250 °C. The film thickness is obtained from the spacing of the oscillations and the surface roughness from the decrease in the signal intensity.

All the platinum films grown from $MeCpPtMe_3$ had a highly preferred (111) orientation.[II,VI] The crystallinity of the films and the proportion of the (111) oriented crystals increased with increasing growth temperature. The (111) orientation is favorable because it has the lowest surface energy of the fcc crystal planes. TEM studies on platinum films grown at 300 °C using air as the reactant showed that the films have well-ordered, columnar grain structure.[189] Single spots were detected in the reflection high energy electron diffraction (RHEED) pattern measured from the same platinum film verifying the strong (111) orientation and pronounced ordering of the grains.[194]

$MeCpPtMe_3$ has been used as a precursor also in ALD of platinum on high surface area Al_2O_3 and SiO_2 supports.[39] $MeCpPtMe_3$ was vaporized at 70 °C which is above its melting point. The supports were exposed to $MeCpPtMe_3$ at 100 °C; $MeCpPtMe_3$ was found to react with the surface hydroxyl groups of the supports already at 100 °C. X-ray photoelectron spectroscopy (XPS) analysis showed that there is platinum with oxidation states of 0 and +2 on the surface. Carbon content analysis of the chemisorbed platinum precursor indicated that during adsorption the three methyl ligands were released as methane in reaction with the hydroxyl groups, and that the MeCp ligands remain on the surface. The remaining ligands were removed from the surface by a separate calcination step at 350 °C in air. During the calcination, part of the platinum at an oxidation state +2 was oxidized to an oxidation state +4. Platinum was reduced in an additional reduction step at 300 °C in hydrogen. However, although the amount of metallic platinum increased during the reduction step, some platinum with an oxidation state of +2 was still left on the surface.[39]

Pt(acac)₂[VIII,192]

Another precursor studied for ALD of platinum is $Pt(acac)_2$.[VIII,192] Both hydrogen and oxygen have been studied as reactive gases. In the hydrogen-based process, $Pt(acac)_2$ was sublimated at 155 °C, but it was found to thermally decompose on the glass walls of the source furnace during sublimation. The hydrogen flow rate was 30 sccm. Platinum films were obtained at 250 °C on titanium, aluminum, and glass substrates. On silicon, only weak indications of film growth were detected.[192] Because of the thermal self-decomposition of $Pt(acac)_2$, self-limiting growth mechanism is hardly achieved in this process.

In the oxygen-based process, $Pt(acac)_2$ was sublimated at slightly lower temperature of 120 °C.[VIII] The oxygen flow rate was 20 sccm. However, only non-uniform films were obtained at the temperature range of 210–220 °C.[VIII]

4.1.3 Iridium

ALD processes for iridium have been reported so far only for $Ir(acac)_3$ and oxygen,[V,VI] and for $Ir(acac)_3$ and hydrogen.[38] Table 4 presents a summary of these iridium ALD processes.

Table 4. Summary of the reported iridium ALD processes.

Metal precursor	$T_{vaporization}$ (°C)	Reaction gas	Flow rate (sccm)	T_{growth} (°C)	Ref.
$Ir(acac)_3$	150	Air	5–40	225–400	**V**
	150	O_2	5–20	225–300	**VI**
	N/A	H_2	separate reduction step	200–250 / 275–450	38

$Ir(acac)_3$[V,VI,38]

$Ir(acac)_3$ is solid at room temperature and has a relatively low vapor pressure,[195] which, however, is not a problem in ALD. In the oxygen-based process, $Ir(acac)_3$ was sublimated at 150 °C. Air with a flow rate of 5–40 sccm or pure oxygen with a flow rate of 5–20 sccm was used as the oxygen source.[V,VI] The film growth took place on Al_2O_3 surface at temperatures of 225 °C and higher. At 400 °C, signs of thermal self-decomposition of $Ir(acac)_3$ were observed, and therefore, 375 °C was considered the upper temperature limit for the process. The temperature range for the film growth is in good accordance with the reported thermal stability of $Ir(acac)_3$ in vacuum and in oxygen atmosphere.[180]

At 300 °C, the growth rate of the iridium films grown from $Ir(acac)_3$ and air saturated to 0.40 Å/cycle as the precursor pulse times were increased.[V] The growth rate depended on the growth temperature; the growth rate increased from 0.23 Å/cycle at 225 °C to 0.55 Å/cycle at 375 °C. For films grown at 300 °C, the film thickness depended linearly on the number of the growth cycles at the studied thickness range of 9–175 nm. Resistance measurements by a four-point-probe indicated that a 9-nm iridium film was already continuous. AFM analysis showed that the films had very smooth surfaces and no notable surface roughening was observed even at high growth temperatures or at high air flow

rates. The surface roughnesses of 9-nm and 65-nm films grown at 300 °C were 0.5 and 1.6 nm, respectively.[V]

Resistivities of about 70-nm thick iridium films grown from $Ir(acac)_3$ and air at temperatures between 225 and 400 °C were lower than 12 $\mu\Omega$·cm.[V] The film resistivity decreased with increasing growth temperature which was most probably due to increased crystallinity of the films. At 400 °C, there was a small increase in the resistivity, possibly due to the increased impurity contents of the film. Figure 13 shows the dependence of the resistivity on the film thickness. The increase in the resistivity with decreasing film thickness is related to an increased effect of grain boundary and surface scattering.[163,174]

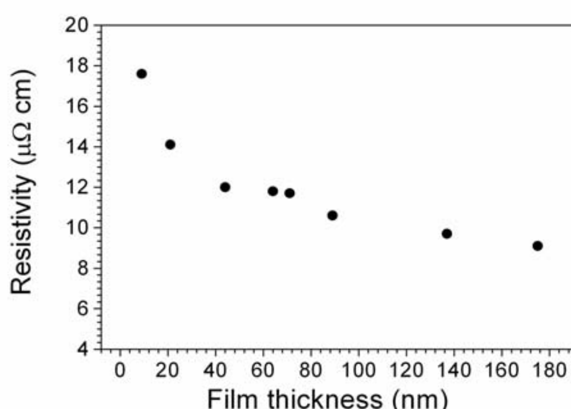

Figure 13. Resistivity of the iridium films grown from $Ir(acac)_3$ as a function of the film thickness. The films were grown at 300 °C.

The iridium films grown from $Ir(acac)_3$ and oxygen at temperatures of 225–400 °C were metallic iridium with a preferred (111) crystal orientation as studied by XRD. The films showed a strong tendency to orient the (111) crystal plane, which has the lowest surface energy, parallel to the surface.[V,VI] Similar tendency was also observed with platinum, which is a fcc metal, too. The iridium films had a preferred (111) crystal orientation even at the lowest growth temperatures[V,VI] implying high surface mobility of the iridium atoms. Figure 14 shows that the (111) crystal orientation is favorable already at the beginning of the growth of an iridium film at 300 °C; in the XRD pattern measured from a 9-nm film, the intensity ratio of the iridium (111) and (200) reflections is 4.6 : 1 while in a randomly oriented powder, the intensity ratio would be 2 : 1.[21]

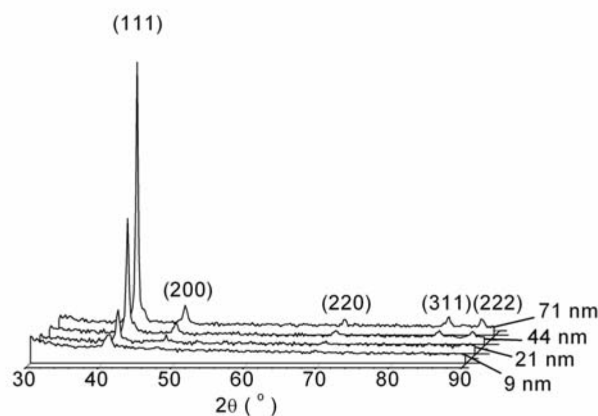

Figure 14. XRD patterns measured from iridium films of different thicknesses. The films were grown at 300 °C.

The impurity contents of the iridium films grown from $Ir(acac)_3$ and oxygen were low as analyzed by TOF-ERDA.[V] The films grown at temperatures of 225–350 °C contained less than 1.0 at. % hydrogen, less than 0.3 at. % carbon, and less than 0.5 at. % oxygen. The film grown at 400 °C had higher oxygen and carbon contents, which is most probably related to the thermal self-decomposition of $Ir(acac)_3$. The iridium films had good adhesion to as-deposited Al_2O_3 and TiN layers, and to silicon with native oxide. Partial oxidation of iridium to iridium oxide took place during post-annealing at 600 °C in oxygen.[V]

Iridium has been deposited by ALD from $Ir(acac)_3$ and hydrogen on large surface area Al_2O_3 and SiO_2-Al_2O_3 supports for catalytic applications.[38] The reaction temperature during $Ir(acac)_3$ exposure was 200 or 250 °C. The results imply that when $Ir(acac)_3$ adsorbs on the support surface, one of the three acac ligands is released in reaction with the surface hydroxyl groups. The remaining ligands were removed by a separate reduction step at temperature of 275–450 °C.[38]

4.1.4 Palladium

ALD of palladium has been reported from $Pd(hfac)_2$ (hfac = hexafluoroacetylacetonato) using hydrogen or glyoxylic acid [HC(O)C(O)OH] as reducing agent.[177] ALD of palladium from $Pd(thd)_2$[VIII,37] and from $Pd(keim2)_2$ {keim2 = $[CF_3C(O)CHC(NBu^n)CF_3]^-$}[VI] has also been studied. The studied palladium ALD processes are summarized in Table 5.

Table 5. Summary of the reported palladium ALD processes.

Metal precursor	$T_{vaporization}$ (°C)	Reaction gas	Flow rate (sccm)	T_{growth} (°C)	Ref.
$Pd(hfac)_2$	50	H_2	8	80, 130	177
		glyoxylic acid + Ar carrier	15	210	
$Pd(thd)_2$	180	H_2	separate reduction step	180/90, 180/300	37
	130	O_2	10–20	250–275	**VIII**
$Pd(keim2)_2$	60	O_2	20, 40	250–275	**VI**

$Pd(hfac)_2$[177]

Palladium has been grown by ALD from $Pd(hfac)_2$ by using two different reducing agents: hydrogen and glyoxylic acid.[177] The sublimation temperature of $Pd(hfac)_2$ was 50 °C, which is below its melting point of 100 °C.[196] Hydrogen had a flow rate of 8 sccm, and glyoxylic acid was vaporized at 60 °C and transported to the reactor by argon carrier with a flow rate of 15 sccm. The process with hydrogen took place on iridium surface at low temperatures of 80–130 °C. Glyoxylic acid had sufficient reactivity only at temperatures higher than 200 °C. An upper temperature limit for the film growth was 230 °C because of the thermal self-decomposition of $Pd(hfac)_2$. With the hydrogen-based process, films were grown on iridium surfaces. Growth rates of 0.26 and 0.13 Å/cycle were obtained at growth temperatures of 80 and 130 °C. The lower growth rate at 130 °C was explained by desorption of $Pd(hfac)_2$ from the palladium surface. At 130 °C, the initial growth rate on the iridium surface was higher than on the as-grown palladium surface. Thus, the growth rate decreased as the initial iridium surface was covered by palladium. The difference in the growth rates was explained by different Ir–$Pd(hfac)_2$ and Pd–$Pd(hfac)_2$ bond energies. The palladium films grown on nearly randomly oriented iridium had a preferred (111) orientation. Palladium seed layers were also grown on tetrasulfide-terminated self-assembled monolayers (SAMs) at 210 °C using glyoxylic acid as a reducing agent. The desorption rate of $Pd(hfac)_2$ increases with increasing temperature, and lower growth rates were obtained in the glyoxylic acid process than in the hydrogen-based process taking place at lower temperatures. The films grown on SAMs at 210 °C had higher carbon and fluorine impurity contents than the films grown on iridium at lower temperatures, which was attributed to the increased dissociation of the hfac ligand at the higher growth temperature.[177]

Pd(thd)$_2$ [VIII,37]

Palladium has been deposited by ALD from Pd(thd)$_2$ on large surface area Al_2O_3 and SiO_2 supports using hydrogen as a reducing agent.[37] In these experiments, only one growth cycle of palladium was applied. Pd(thd)$_2$, which has melting point of 255 °C, was sublimated at 180 °C. The supports were exposed to Pd(thd)$_2$ at the same temperature. During adsorption on Al_2O_3 and SiO_2, the thd ligands of the palladium precursor reacted with the hydroxyl groups of the surface, and desorbed from the surface as Hthd. Most of the thd ligands were lost already during Pd(thd)$_2$ adsorption. The adsorbed precursor was reduced by a separate reducing step at 90 °C or at 300 °C leading to an additional decrease of the amount of the ligands on the surface. However, even after the reduction step, a small portion of the ligands remained on the surface. In addition, the deposits also contained oxidized palladium. Pd(thd)$_2$ was found to be more reactive towards the SiO_2 surface than the Al_2O_3 surface, which may be related to a higher density of hydroxyl groups on the SiO_2 surface.[37]

ALD of palladium from Pd(thd)$_2$ has also been studied in an oxygen-based process.[VIII] The sublimation temperature of Pd(thd)$_2$ was 130 °C, and the growth temperatures studied were 250 and 275 °C. However, only non-uniform films were obtained; the films were thicker at the trailing edge of the substrate suggesting that etching of the film by the incoming palladium precursor may possibly take place.[VIII]

Pd(keim2)$_2$ [VI]

ALD of palladium from a β-ketoiminato compound Pd(keim2)$_2$ and oxygen has been studied as well.[VI] Pd(keim2)$_2$ was vaporized at 60 °C which also is its melting point.[197] The growth temperatures were 250 and 275 °C.[VI] As studied by XRD, the films were metallic palladium with a preferred (111) orientation. The growth rate did not saturate to a constant value at the studied pulse time range of 0.5–2 s. The lack of saturation may be either due to poor reactivity of the precursors, or to thermal self-decomposition of Pd(keim2)$_2$. However, the impurity contents of the films determined by TOF-ERDA were relatively low; the films contained 0.3 at.% hydrogen, 0.5 at.% carbon, 0.1 at.% nitrogen, 1.0 at.% oxygen, and 0.1 at.% fluorine. The films had poor adhesion to Al_2O_3 but adhered well to a thin, as-grown iridium film. Although palladium films with good quality could be grown, the process cannot be considered true ALD process because self-limiting film growth was not obtained.[VI]

4.1.5 Rhodium

So far, there are only a few reports on ALD of rhodium; ALD of rhodium from $CpRh(CO)_2$ and oxygen has been reported in patent literature,[178] and ALD of rhodium from $Rh(acac)_3$ and oxygen is reported in Paper VII. Table 6 summarizes the reported rhodium ALD processes.

Table 6. Summary of the reported rhodium ALD processes.

Metal precursor	$T_{vaporization}$ (°C)	Reaction gas	Flow rate (sccm)	T_{growth} (°C)	Ref.
$CpRh(CO)_2$	N/A	O_2	50	100	178
$Rh(acac)_3$	150	O_2	10–20	200–300	**VII**

$CpRh(CO)_2$[178]

An oxygen-based ALD process has been reported for rhodium from $CpRh(CO)_2$, which is a liquid at room temperature.[178] Growth of metallic rhodium takes place at low temperature of 100 °C with $CpRh(CO)_2$ flow rate of 5 sccm and oxygen flow rate of 50 sccm.[178] Rhodium oxide RhO_2 is obtained when ozone is used as the reaction gas.[198] Metallic rhodium films can be oxidized to RhO_2 by annealing in oxygen at 850 °C for 30 s.[198]

$Rh(acac)_3$[**VII**]

Rhodium films have been grown from $Rh(acac)_3$ and oxygen.[**VII**] $Rh(acac)_3$ was sublimated at 150 °C, which is below its melting point of 260 °C.[199] The vapor pressure of $Rh(acac)_3$ is relatively low at 150 °C, and therefore, relatively long pulse times were needed. $Rh(acac)_3$ was sublimated at as low temperature as possible to avoid its decomposition during sublimation. The films were grown at a temperature range of 200–300 °C. At 300 °C, $Rh(acac)_3$ showed signs of thermal self-decomposition, and therefore, it can be considered the upper limit for the growth temperature. At 250 °C, a growth rate of 0.75 Å/cycle was obtained with oxygen pulse times of 1–10 s. The growth rate depended somewhat on the $Rh(acac)_3$ pulse time but seemed to stabilize to about 0.80 Å/cycle at long pulse times. The low vapor pressure of $Rh(acac)_3$ explain the long pulse times needed to obtain saturation. The slight increase in the growth rate with increasing $Rh(acac)_3$ pulse time may also be related to thermal self-decomposition of $Rh(acac)_3$, or to its adsorption/desorption behavior.[**VII**] The growth rates obtained in this process are relatively

high as compared to the other oxygen-based noble metal ALD processes.[VIII] The thickness of the films depended linearly on the number of the growth cycles.[VII]

The films grown from $Rh(acac)_3$ and oxygen at 250 °C were metallic rhodium with a preferred (111) crystal orientation as analyzed by XRD.[VII] TOF-ERD analysis showed that the films contained less than 0.1 at.% hydrogen, 1.6 at.% carbon, and 2.3 at.% oxygen. Films thicker than 20 nm had resistivities less than 12 $\mu\Omega\cdot$cm. Adhesion of the films to Al_2O_3 was relatively good; only films thicker than 80 nm did not pass the tape test.[VII]

4.2 Reaction mechanisms

There are only a few studies on the reaction mechanisms of the noble metal ALD processes.[III,IV,37,39,177] All these studies apply to conventional, thermally activated ALD processes. Reaction mechanisms of the plasma-assisted noble metal ALD processes are apparently more complicated and have not been studied so far. While considering reaction mechanisms, one must distinguish between the reactions taking place on the initial growth surface and the reactions taking place on the surface of the as-deposited noble metal film. Furthermore, the catalytic nature of the noble metals must be taken into account when studying reactions on noble metal surfaces.

4.2.1 Oxidizing processes

Reaction mechanisms of the oxygen-based noble metal ALD processes taking place on the as-deposited noble metal surface have been studied *in situ* by a quadrupole mass spectrometer (QMS) and quartz crystal microbalance (QCM).[III,IV] The QMS studies on ALD of ruthenium from $RuCp_2$ and ALD of platinum from $MeCpPtMe_3$ show that the ligands become oxidized mainly to water and carbon dioxide.[III] These reaction by-products are detected during both the metal precursor pulse and the oxygen pulse. Thus, on the surface, there must be chemisorbed oxygen during the metal precursor pulse and unreacted ligand species during the oxygen pulse. Figure 15 shows the proposed reaction mechanism; oxygen chemisorbs on the metal surface during the oxygen pulse, and the ligands of the metal precursor react with this chemisorbed oxygen during the following metal precursor pulse.[III] Because of the limited amount of the chemisorbed oxygen, the ligands do not become completely oxidized but some unreacted ligand species remain on the surface after the metal precursor pulse. These species then react with oxygen during the following oxygen pulse.[III] In the $RuCp_2$ process, the ligands reacted with oxygen to produce mainly

water and carbon dioxide while in the $Ru(thd)_3$ process, also carbon monoxide and hydrogen were detected.[IV] Thus, the reactions taking place on the noble metal surface depend on the chemical nature of the ligands of the metal precursor.

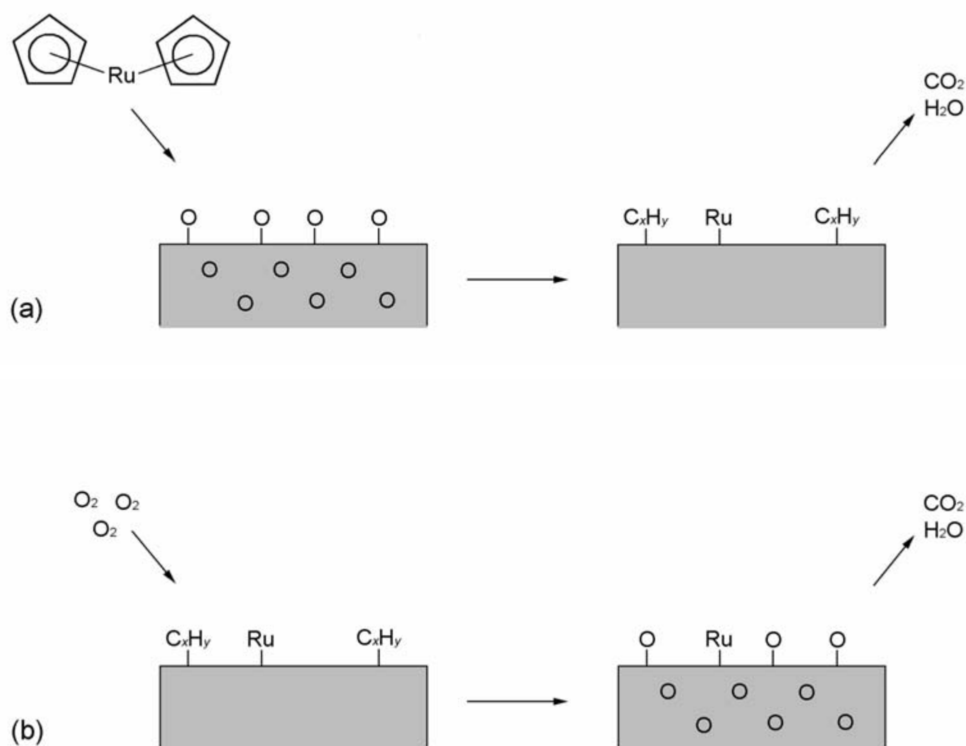

Figure 15. Reactions taking place on the ruthenium surface (a) during the $RuCp_2$ pulse and (b) during the O_2 pulse.

The *in situ* QCM studies show that during the $RuCp_2$ pulse there is a momentary mass increase at the beginning of the pulse but that the total mass change is negative (*i.e.* the mass decreases). Respectively, during the oxygen pulse, the total mass change is positive (*i.e.* the mass increases).[III] The mass increase during the oxygen pulse can be explained by chemisorption of oxygen on the ruthenium surface and diffusion of oxygen atoms to the subsurface region. During the $RuCp_2$ pulse, the $RuCp_2$ precursor first chemisorbs on the surface leading to a mass increase. After that, as the ligands start to react with the chemisorbed oxygen atoms, volatile reaction products leave the surface, and the mass starts to decrease. On the basis of the QMS studies, it can be estimated that about 15 oxygen atoms are consumed per one chemisorbing $RuCp_2$ molecule.[III] The mass change calculated on the basis of the QMS results is negative during the $RuCp_2$ pulse, and in relatively good agreement with the mass decrease detected by QCM.[III] The growth rate of the ruthenium

films grown from $RuCp_2$ at 350 °C corresponds to 0.2 monolayers (ML) of ruthenium per one growth cycle.[I] Thus, 15 oxygen atoms per one deposited ruthenium atom corresponds to an oxygen atom amount equal to 3 ML.[III] Figure 16 shows the relative sizes of the ruthenium atoms[21] and the Cp ligands.[200]

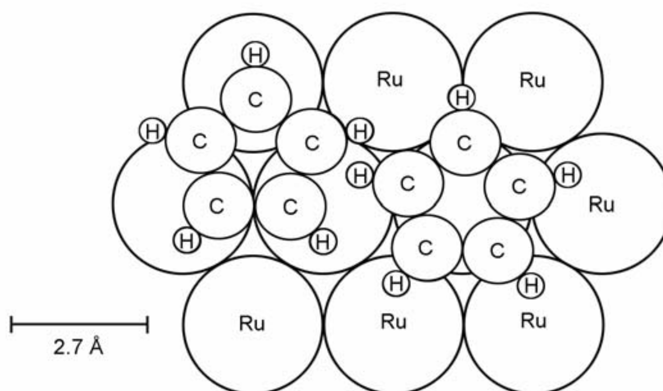

Figure 16. Relative sizes of the ruthenium atoms and the Cp ligands.

The *in situ* QMS and QCM analysis of the ruthenium and platinum processes show that chemisorption of oxygen on the noble metal surface plays an important role in the reaction mechanisms. Oxygen chemisorption on most of the noble metals is dissociative, that is, oxygen binds to the surface as separate atoms. Dissociation of the oxygen molecule to oxygen atoms increases its reactivity; the as-deposited noble metal films thus self-catalyze the film growth reactions.

On ruthenium, ultra high vacuum (UHV) studies have shown that dissociative chemisorption of oxygen takes place below room temperature, and at temperatures higher than 280 °C, oxygen atoms start to penetrate into the subsurface region.[18] The oxygen atoms in the subsurface layer are in the form of dissolved oxygen, not in the form of covalently bound ruthenium oxide. Thus, the subsurface oxygen is mobile and can participate in surface reactions. The amount of oxygen in the adsorption layer depends on the temperature and on the oxygen partial pressure.[18] A stable RuO_2 phase forms only at temperatures higher than 480 °C.[18]

The growth rate of the ruthenium films grown by ALD has been reported to depend on the oxygen partial pressure,[156] and on the growth temperature.[I,II] These dependencies may be related to the amount of adsorbed oxygen on ruthenium; more oxygen adsorbs on ruthenium at high oxygen partial pressures and at high substrate temperatures. Hence, higher portion of the precursor ligands are consumed in the reaction with the chemisorbed

oxygen, and due to the increased number of free adsorption sites, more ruthenium precursor molecules are able to chemisorb on the surface. It has been shown that if the chemisorbed oxygen atoms are removed by a hydrogen plasma, lower growth rates are obtained.[201] The observation that ruthenium films are obtained although oxygen is removed from the surface suggests that a chemisorbed oxygen layer is not a prerequisite for the film growth to proceed.

According to the reaction mechanism presented in Figure 15 for ALD of ruthenium, all oxygen in the adsorption layer is consumed during the ruthenium precursor pulse. Lack of ruthenium oxide formation and the low oxygen content of the films[I,IV] support this mechanism. However, some oxygen may remain in the subsurface layer if the amount of adsorbed oxygen in the subsurface layer is high, if the noble metal precursor dose is deficient, or if the noble metal precursor pulse time is too short for the reactions to proceed to completion. In such cases, some oxygen may remain in the subsurface layer. In fact, ruthenium oxide has been obtained ALD with high oxygen partial pressures and short ruthenium precursor pulse times.[156]

On platinum, dissociative chemisorption of oxygen takes place at UHV below room temperature, and associative desorption of oxygen occurs at temperatures higher than 330 °C.[202] A subsurface oxygen layer has also been reported to form on platinum surface,[203,204] but it is much more unlikely than on ruthenium surface. The subsurface oxygen is also less reactive than the surface oxygen.[203] Platinum oxide starts to form at temperatures higher than 530 °C.[17] On iridium, dissociative chemisorption of oxygen takes place already at room temperature, and diffusion of oxygen into the subsurface region begins at temperatures higher than 30 °C.[205] An initial stage of iridium surface oxidation has been observed at 330 °C, and more intensive oxidation takes place at temperatures higher than 580 °C.[205]

On palladium surface, dissociative chemisorption of oxygen takes place at UHV at temperatures below the room temperature.[206] Associative desorption of oxygen, on the other hand, takes place at temperatures higher than 480 °C. Oxygen also migrates into the subsurface region but even at 250 °C the formation of the subsurface oxide is relatively slow and the amount of oxygen in the subsurface region is small.[206] The reactivity of the subsurface oxygen is lower than that of chemisorbed oxygen on the palladium surface.[206] During oxygen exposure at temperatures higher than 200 °C, surface oxidation of palladium to PdO may also take place.[207] On rhodium, dissociative chemisorption of

oxygen takes place below room temperature, and subsurface oxygen starts to form at 100 °C at UHV.[208] Desorption of the subsurface oxygen begins at 380 °C.[208]

The film growth must take place not only on the as-deposited noble metal surface but also on the initial substrate surface. The chemical nature of the initial substrate surface may be very different to that of the noble metal surface, and in particular, it may not have catalytic activity for oxygen dissociation. Only after the substrate is partly or fully covered by the noble metal, the reaction mechanisms change to those taking place on the as-deposited noble metal surface. The reactions with the initial substrate surface are very important because they may limit the onset-temperature for the film growth or even totally prohibit the film growth. Ruthenium films, for example, were obtained at lower growth temperatures on iridium than on as-deposited Al_2O_3.[**VI**] The catalytic activity of the iridium surface enables onset of the ruthenium film growth at lower temperatures than on Al_2O_3. Thus, poor reactivity of the precursors on the initial Al_2O_3 surface restricts the film growth at low temperatures.

4.2.2 Reducing processes

Hydrogen-based ALD processes have been studied for ruthenium,[37] platinum,[39,192] iridium,[38] and palladium.[37,177] Other reducing agents reported for thermally activated noble metal ALD processes include glyoxylic acid[177] and hydrazine.[187] In hydrogen-based processes taking place on noble metal surfaces, dissociative chemisorption of hydrogen catalytically activates the reactions; the ligands are released from the surface in the hydrogenated form, and the central metal ion is reduced to metallic state.[177] Stability of the chemisorbed noble metal precursor against desorption is essential; in ALD of palladium from $Pd(hfac)_2$, desorption rate of the noble metal precursor increases with increasing substrate temperature leading to a lower growth rate.[177]

Reactions of the β-diketonate precursors $Pd(thd)_2$, $Ru(thd)_3$, and the cyclopentadienyl precursor $MeCpPtMe_3$ with the hydroxyl groups on high surface area Al_2O_3 and SiO_2 supports have been studied by several analysis methods such as thermogravimetric analysis and mass spectrometry.[37,39] The results show that the both thd ligands of the $Pd(thd)_2$ precursor react with the surface hydroxyl groups. The reaction by-products detected with a mass spectrometer were Hthd and its fragments as well as 2-dimethyl propionic acid.[37] Palladium with oxidation states of 0 and +2, and +6 were detected on the surface by XPS, the metallic state with oxidation number of 0 being the most abundant.[37] The ruthenium

precursor $Ru(thd)_3$ chemisorbs on the surface at 180 °C without losing any ligands. The density of the ruthenium atoms on the surface was very low, probably due to a low reactivity of $Ru(thd)_3$ or to a fast desorption of $Ru(thd)_3$ from the surface.[37] The three methyl ligands in $MeCpPtMe_3$ react with the surface hydroxyl groups but the MeCp ligands remain on the surface. Platinum with oxidation states of 0 and +2 were detected on the surface after the first reaction step.[39] It is possible that the formation of metallic atoms on the surface already during the adsorption of the metal precursor enables catalytic activation of the reduction reaction during the following reduction step. That is, the hydrogen atoms dissociatively adsorb on the metallic atoms, and the reaction thus becomes catalytically activated already during the first growth cycle.

Interaction of $Pd(hfac)_2$ with tetrasulfide-terminated SAMs has been studied by XPS.[177] For the palladium film growth to take place on a SAM, the $Pd(hfac)_2$ molecule must be able to chemisorb on the SAM, that is, an interfacial Pd–S bond must form.[177] Shift in the sulfur peak in the XPS spectrum shows that $Pd(hfac)_2$ indeed chemisorbs on the sulfur atom of the tetrasulfide-terminated SAM.[177] The advantage of being able to grow palladium on SAMs is that SAMs enable modification of the initial growth surface.[177]

5. CONCLUSIONS

The results obtained in this work show that high quality ruthenium, platinum, iridium, and rhodium films can be grown by ALD. ALD of palladium was also studied, but the film growth did not proceed by a self-limiting ALD mechanism. All of the processes are based on reactions of the metal precursor with oxygen, the growth temperatures being in the range of 200–450 °C.

Ruthenium films were grown from two ruthenium precursors: a cyclopentadienyl precursor $RuCp_2$ and a β-diketonato precursor $Ru(thd)_3$. The films grown from $RuCp_2$ had resistivities lower than 20 $\mu\Omega\cdot$cm, and the films grown at 350 °C contained less than 0.2 at.% hydrogen, less than 0.2 at.% carbon, and less than 0.4 at.% oxygen. The film growth rate at 350 °C saturated to 0.45 Å/cycle. The films grown from $Ru(thd)_3$ had higher resistivities, higher impurity contents, and longer incubation time for the onset of the film growth.

Platinum films with a strong (111) orientation were grown from $MeCpPtMe_3$ and oxygen at temperatures of 200–300 °C. The films had low resistivities and low impurity contents; a 30-nm platinum film grown at 200 °C had a resistivity of 17 $\mu\Omega\cdot$cm and contained less than 0.2 at.% of hydrogen, carbon, and oxygen, each. $Pt(acac)_2$ was also studied as a platinum precursor but only non-uniform films were obtained.

Iridium films were grown from $Ir(acac)_3$ and oxygen at a temperature range of 225–375 °C. The films were metallic iridium with a preferred (111) crystal orientation. Depending on the thickness, the films had resistivities in the range of 9–18 $\mu\Omega\cdot$cm. The films had smooth surfaces; a 65-nm film grown at 300 °C had an rms surface roughness of 1.6 nm. At 300 °C, the film growth rate saturated to 0.40 Å/cycle, and the film thickness depended linearly on the number of the growth cycles.

Metallic rhodium films with a preferred (111) crystal orientation were grown from $Rh(acac)_3$ and oxygen at temperature of 250 °C. A 30-nm film had a resistivity of about 10 $\mu\Omega\cdot$cm. The films contained less than 0.1 at.% hydrogen, 1.6 at.% carbon, and 2.3 at.% oxygen.

ALD of palladium was studied from two palladium precursors: a β-ketoiminato precursor $Pd(keim2)_2$ and a β-diketonato precursor $Pd(thd)_2$. Although palladium films with good

quality could be grown from Pd(keim2)$_2$, the process cannot be considered true ALD process because self-limiting film growth was not achieved. The films grown from Pd(thd)$_2$ and oxygen were non-uniform, probably because of etching reactions.

The reaction mechanism studies showed that adsorbed oxygen on the noble metal surface plays an important role in the film growth reactions; oxygen adsorbs on the noble metal surface during the oxygen pulse, and the adsorbed oxygen atoms react with the ligands of the noble metal precursor during the following metal precursor pulse. Because of the limited amount of adsorbed oxygen in the adsorption layer, some unreacted ligand species remain on the surface. These species react with oxygen during the next oxygen pulse. The main reaction by-products were water and carbon dioxide. Since only traces of impurities were detected in the films, the surface reactions go to completion.

On the basis of the studied processes, it can be concluded that the oxidizing chemistry works well with the different metals and with the different types of metal precursors. Despite the oxidizing process condition, the metals did not become oxidized but metallic films were obtained in all process conditions used in this work. Saturation of the film growth rate was observed in most of the processes, showing that adsorption of the precursors was self-limiting.

ALD is a suitable method for growing noble metals for the potential applications in ICs which include electrodes in DRAMs and FRAMs, gate electrodes in MOSFETs, and seed layers for copper in interconnect metallization. Noble metal ALD processes taking place in oxidizing conditions can be used when growing DRAM and FRAM top electrodes, gate electrodes for MOSFETs and ferroelectric FETs, and combined seed and barrier layers for copper in interconnect metallization. The DRAM and FRAM bottom electrodes as well as the copper seed layers grown on nitride barriers need to be grown in reducing process conditions.

All the processes studied in this work take place in oxidizing conditions. In order to be able to grow noble metals on nitride barriers and other easily oxidizing materials, more research is needed on thermal noble metal ALD processes taking place in reducing conditions. Film growth on different kinds of starting surfaces should also be studied; so far, most of the noble metal deposition studies have been performed on Al_2O_3, SiO_2, and noble metal surfaces. The results presented in this thesis are thus likely to be only the opening of research on ALD of noble metals.

6. REFERENCES

I Aaltonen, T., Alén, P., Ritala, M., and Leskelä, M., Ruthenium thin films grown by atomic layer deposition, *Chem. Vap. Deposition*, **9** (2003) 45–49.

II Aaltonen, T., Ritala, M., Sajavaara, T., Keinonen, J., and Leskelä, M., Atomic layer deposition of platinum thin films, *Chem. Mater.*, **15** (2003) 1924–1928.

III Aaltonen, T., Rahtu, A., Ritala, M., and Leskelä, M., Reaction mechanism studies on atomic layer deposition of ruthenium and platinum, *Electrochem. Solid-State Lett.*, **6** (2003) C130–C133.

IV Aaltonen, T., Ritala, M., Arstila, K., Keinonen, J., and Leskelä, M., Atomic layer deposition of ruthenium thin films from $Ru(thd)_3$ and oxygen, *Chem. Vap. Deposition*, **10** (2004) 215–219.

V Aaltonen, T., Ritala, M., Sammelselg, V., and Leskelä, M., Atomic layer deposition of iridium thin films, *J. Electrochem. Soc.*, **151** (2004) G489–G492.

VI Aaltonen, T., Ritala, M., Tung, Y.-L., Chi, Y., Arstila, K., Meinander, K., and Leskelä, M., Atomic layer deposition of noble metals: Exploration of the low limit of the deposition temperature, *J. Mater. Res.*, **19** (2004) 3353–3358.

VII Aaltonen, T., Ritala, M., and Leskelä, M., Atomic layer deposition of rhodium thin films from $Rh(acac)_3$ and oxygen, manuscript.

VIII Aaltonen, T., Ritala, M., and Leskelä, M., Atomic layer deposition of noble metals, in *Advanced Metallization Conference 2004 (AMC 2004),* (Eds: D. Erb, P. Ramm, K. Masu, and A. Osaki), Materials Research Society (2005) 663–667.

1. Suntola, T., Method for producing compound thin films, *U.S. Patent*, US4058430 (1977).
2. Suntola, T., Antson, J., Pakkala, A., and Lindfors, S., Atomic layer epitaxy for producing EL-thin films, *SID 80 Dig.*, **11** (1980) 108–109.
3. Suntola, T., Atomic layer epitaxy, *Thin Solid Films*, **216** (1992) 84–89.
4. Ritala, M. and Leskelä, M., Atomic layer deposition, in *Handbook of Thin Film Materials*, (Ed: H. S. Nalwa), **1**, Academic Press, San Diego, CA (2002) 103–159.
5. Hsu, C. T., Epitaxial growth of II–VI compound semiconductors by atomic layer epitaxy, *Thin Solid Films*, **335** (1998) 284–291.
6. Arès, R., Watkins, S. P., Yeo, P., Horley, G. A., O'Brien, P., and Jones, A. C., Growth mechanism in atomic layer epitaxy of GaAs, *J. Appl. Phys.*, **83** (1998) 3390–3397.
7. Lakomaa, E.-L., Atomic layer epitaxy (ALE) on porous substrates, *Appl. Surf. Sci.*, **75** (1994) 185–196.
8. Haukka, S., Lakomaa, E.-L., and Suntola, T., Adsorption controlled preparation of heterogeneous catalysts, *Stud. Surf. Sci. Catal.*, **120** (1998) 715–750.
9. Rosental, A., Tarre, A., Gerst, A., Sundqvist, J., Hårsta, A., Aidla, A., Aarik, J., Sammelselg, V., and Uustare, T., Gas sensing properties of epitaxial SnO_2 thin films prepared by atomic layer deposition, *Sens. Actuators B*, **93** (2003) 552–555.
10. Ritala, M. and Leskelä, M., Atomic layer deposition of thin films for microelectronics, *Electrochem. Soc. Proc.*, **2003-08** (2003) 479–490.
11. Ritala, M., Leskelä, M., Dekker, J.-P., Mutsaers, C., Soininen, P. J., and Skarp, J., Perfectly conformal TiN and Al_2O_3 films deposited by atomic layer deposition, *Chem. Vap. Deposition*, **5** (1999) 7–9.

12. Kim, H., Atomic layer deposition of metal and nitride thin films: current research efforts and applications for semiconductor device processing, *J. Vac. Sci. Technol. B*, **21** (2003) 2231–2261.
13. Klaus, J. W., Ferro, S. J., and George, S. M., Atomic layer deposition of tungsten using sequential surface chemistry with a sacrificial stripping reaction, *Thin Solid Film*, **360** (2000) 145–153.
14. Mårtensson, P. and Carlsson, J.-O., Atomic layer epitaxy of copper, growth and selectivity in the Cu(II)-2,2,6,6-tetramethyl-3,5-heptanedionate/H_2 process, *J. Electrochem. Soc.*, **145** (1998) 2926–2931.
15. Solanki, R. and Pathangey, Atomic layer deposition of copper seed layers, *Electrochem. Solid-State Lett.*, **3** (2000) 479–480.
16. *CRC Handbook of Chemistry and Physics* (Ed: D. R. Lide), 82nd ed., CRC Press, Boca Raton, FL (2001) 12-219–12-220.
17. Gland, J. L., Sexton, B. A., and Fisher, G. B., Oxygen interactions with the Pt(111) surface, *Surf. Sci.*, **95** (1980) 587–602.
18. Böttcher, A. and Niehus, H., Formation of subsurface oxygen at Ru(0001), *J. Chem. Phys.*, **110** (1999) 3186–3195.
19. Kohli, S., Rithner, C. D., and Dorhout, P. K., X-ray characterization of annealed iridium films, *J. Appl. Phys.*, **91** (2002) 1149–1154.
20. *CRC Handbook of Chemistry and Physics* (Ed: D. R. Lide), 82nd ed., CRC Press, Boca Raton, FL (2001) 8-21–8-26, 12-45–12-47, and 12-130.
21. International Centre for Diffraction Data (ICDD), **PDF2_47**, Pennsylvania, PA (1997) Cards No. 6-0663, 6-0662, 5-0685, 6-0598, 46-1043, 4-0802, 4-0783, 41-1402, and 4-0784.
22. Serp, P., Chateau, L., Feurer, R., Kiennemann, A., and Kalck, P., Rhodium-catalyzed hydrocarbonylation of acetic acid into higher acids, *J. Mol. Catal. A*, **136** (1998) 269–278.
23. Bond, G. C. and Thompson, D. T., Catalysis by gold, *Catal. Rev. Sci. Eng.* **41** (1999) 319–388.
24. Breen, J. P., Burch, R., Gomez-Lopez, J., Griffin, K., and Hayes, M., Steric effects in the selective hydrogenation of cinnamaldehyde to cinnamyl alcohol using an Ir/C catalyst, *Appl. Catal. A*, **268** (2004) 267–274.
25. Kennedy, D. R., Webb, G., Jackson, S. D., and Lennon, D., Propyne hydrogenation over alumina-supported palladium and platinum catalysts, *Appl. Catal. A*, **259** (2004) 109–120.
26. Waterhouse, G. I. N., Bowmaker, G. A., and Metson, J. B., Influence of catalyst morphology on the performance of electrolytic silver catalysts for the partial oxidation of methanol to formaldehyde, *Appl. Catal. A*, **266** (2004) 257–273.
27. Song, Z., Cai, T., Hanson, J. C., Rodriguez, J. A., and Hrbek, J., Structure and reactivity of Ru nanoparticles supported on modified graphite surfaces: a study of the model catalyst for ammonia synthesis, *J. Am. Chem. Soc.*, **126** (2004) 8576–8584.
28. Shelef, M. and McCabe, R. W., Twenty-five years after introduction of automotive catalysts: What next?, *Catal. Today*, **62** (2000) 35–50.
29. Amiridis, M. D., Mihut, C., Maciejewski, M., and Baiker, A., The selective catalytic reduction of NO by hydrocarbons over Pt- and Ir-based catalysts, *Top. Catal.*, **28** (2004) 141–150.
30. Richter, M., Fricke, R., and Eckelt, R., Unusual activity enhancement of NO conversion over Ag/Al_2O_3 by using a mixed NH_3/H_2 reductant under lean conditions, *Catal. Lett.*, **94** (2004) 115–118.
31. Liguras, D. K., Kondarides, D. I., and Verykios, X. E., Production of hydrogen for fuel cells by steam reforming of ethanol over supported noble metal catalysts, *Appl. Catal. B*, **43** (2003) 345–354.

32. Ghenciu, A. F., Review of fuel processing catalysts for hydrogen production in PEM fuel cell systems, *Curr. Opin. Solid State Mater. Sci.*, **6** (2002) 389–399.
33. Metha, V. and Cooper, J. S., Review and analysis of PEM fuel cell design and manufacturing, *J. Power Sources*, **114** (2003) 32–53.
34. McNicol, B. D., Rand, D. A. J., and Williams, K. R., Direct methanol–air fuel cells for road transportation, *J. Power Sources*, **83** (1999) 15–31.
35. Hogarth, M. P. and Ralph, T. R., Catalysis for low temperature fuel cells, *Platinum Metals Rev*., **46** (2002) 146–164.
36. Serp, P., Kalck, P., and Feurer, R., Chemical vapor deposition methods for the controlled preparation of supported catalytic materials, *Chem. Rev.*, **102** (2002) 3085–3128.
37. Lashdaf, M., Hatanpää, T., Krause, A. O. I., Lahtinen, J., Lindblad, M., and Tiitta, M., Deposition of palladium and ruthenium β-diketonates on alumina and silica supports in gas and liquid phase, *Appl. Catal. A*, **241** (2003) 51–63.
38. Jylhä, O., Saarinen, R., Lindblad, M., and Krause, O., Iridium on porous supports prepared by ALD for heterogeneous catalysis applications, *ALD 2004*, Helsinki, August 16-18 (2004).
39. Lashdaf, M., Lahtinen, J., Lindblad, M., Venäläinen, T., and Krause, A. O. I., Platinum catalysts on alumina and silica prepared by gas- and liquid-phase deposition in cinnamaldehyde hydrogenation, *Appl. Catal. A*, **276** (2004) 129–137.
40. Hemphill, R., Hurwitz, M., and Pelizzo, M. G., Osmium atomic-oxygen protection by an iridium overcoat for increased extreme-ultraviolet grating efficiency, *Appl. Opt*., **42** (2003) 5149–5157.
41. Larruquert, J. I., Méndez, J. A., and Aznárez, J. A., Nonoxidized Al-overcoated Ir bilayers with a high reflectance in the extreme ultraviolet above 50 nm, *Opt. Eng.*, **41** (2002) 1418–1424.
42. Igumenov, I. K., Gelfond, N. V., Galkin, P. S., Morozova, N. B., Fedotova, N. E., Zharkova, G. I., Shipachev, V. I., Reznikova, E. F., Ryabtsev, A. D., Kotsupalo, N. P., Titarenko, V. I., Dikov, Y. P., Distler, V. V., and Buleev, M. I., Corrosion testing of platinum metals CVD coated titanium anodes in seawater-simulated solutions, *Desalination*, **136** (2001) 273–280.
43. Jun, C.-S. and Lee, K.-H., Palladium and palladium alloy composite membranes prepared by metal-organic chemical vapor deposition method (cold-wall), *J. Membr. Sci.*, **176** (2000) 121–130.
44. Kajiwara, M., Uemiya, S., Kojima, T., and Kikuchi, E., Rhodium- and iridium-dispersed porous alumina membranes and their hydrogen permeation properties, *Catal. Today*, **56** (2000) 83–87.
45. Briand, D., van der Schoot, B., de Rooij, N. F., Sundgren, H., and Lundström, I., A low-power micromachined MOSFET gas sensor, *J. Microelectromech. Syst.*, **9** (2000) 303–307.
46. Zimmer, M., Burgmair, M., Scharnagl, K., Karthigeyan, A., Doll, T., and Eisele, I., Gold and platinum as ozone sensitive layer in work-function gas sensor, *Sens. Actuators B*, **80** (2001) 174–178.
47. Kuban, P., Berg, J. M., Dasgupta, P. K., Durable microfabricated high-speed humidity sensors, *Anal. Chem.*, **76** (2004) 2561–2567.
48. Pijolat, C., Riviere, B., Kamionka, M., Viricelle, J. P., and Breuil, P., Tin dioxide gas sensor as a tool for atmospheric pollution monitoring: problems and possibilities for improvements, *J. Mater. Sci.*, **38** (2003) 4333–4346.
49. Abarra, E. N., Inomata, A., Sato, H., Okamoto, I., and Mizoshita, Y., Longitudinal magnetic recording media with thermal stabilization layers, *Appl. Phys. Lett.*, **77** (2000) 2581–2583.

50. Wang, J. P., Piramanayagam, S. N., Hee, C. H., Huang, L., Pang, S. I., Chow, S. K., Shi, X., and Chong, T. C., Design of laminated antiferromagnetically coupled media for beyond 100 Gb/in^2 areal density, *J. Appl. Phys.*, **91** (2002) 7694–7696.
51. Slaughter, J. M., Dave, R. W., DeHerrera, M., Durlam, M., Engel, B. N., Janesky, J., Rizzo, N. D., and Tehrani, S., Fundamentals of MRAM technology, *J. Supercond.*, **15** (2002) 19–25.
52. Guth, M., Schmerber, G., and Dinia, A., Magnetic tunnel junctions for magnetic random access memory applications, *Mater. Sci. Eng. C*, **19** (2002) 129–133.
53. Colis, S., Guth, M., Arabski, J., and Dinia, A., Thermal stability of spin valve sensors using artificial CoFe/Ir based ferrimagnets, *J. Appl. Phys.*, **91** (2002) 2172–2175.
54. Kotecki, D. E., Baniecki, J. D., Shen, H., Laibowitz, R. B., Saenger, K. L., Lian, J. J., Shaw, T. M., Athavale, S. D., Cabral, Jr., C., Duncombe, P. R., Gutsche, M., Kunkel, G., Park, Y.-J., Wang, Y.-Y., and Wise, R., (Ba,Sr)TiO_3 dielectrics for future stacked capacitor DRAM, *IBM J. Res. Dev.*, **43** (1999) 367–382.
55. Kingon, A. I., Streiffer, S. K., Basceri, C., and Summerfelt, S. R., High-permittivity perovskite thin films for dynamic random-access memories, *MRS Bulletin*, **21(7)** (2004) 46–52.
56. Hwang, C. S., (Ba,Sr)TiO_3 thin films for ultra large scale dynamic random access memory. A review on the process integration, *Mater. Sci. Eng. B*, **56** (1998) 178–190.
57. Yoon, D.-S., Roh, J. S., Baik, H. K., and Lee, S.-M., Future direction for a diffusion barrier in future high-density volatile and nonvolatile memory devices, *Crit. Rev. Solid State Mater. Sci.*, **27** (2002) 143–226.
58. Iwai, H. and Ohmi, S., Silicon integrated circuit technology from past to future, *Microelectron. Reliab.*, **42** (2002) 465–491.
59. Mandelman, J. A., Dennard, R. H., Bronner, G. B., DeBrosse, J. K., Divakaruni, R., Li, Y., and Radens, C. J., Challenges and future directions for the scaling of dynamic random-access memory (DRAM), *IBM. J. Res. Develop.*, **46** (2002) 187–212.
60. Chaneliere, C., Autran, J. L., Devine, R. A. B., and Balland, B., Tantalum pentoxide (Ta_2O_5) thin films for advanced dielectric applications, *Mater. Sci. Eng. R*, **22** (1998) 269–322.
61. Ezhilvalavan, S. and Tseng, T.-Y., Progress in the developments of (Ba,Sr)TiO_3 (BST) thin films for Gigabit era DRAMs, *Mater. Chem. Phys.*, **65** (2000) 227–248.
62. Choi, E.-S., Lee, J.-C., Hwang, J.-S., Park, J.-B., and Yoon, S.-G., Bottom electrode structures of Pt/RuO_2/Ru for integration of (Ba,Sr)TiO_3 thin films on polysilicon, *J. Electrochem. Soc.*, **146** (1999) 4189–4193.
63. Yamamichi, S., Lesaicherre, P.-Y., Yamaguchi, H., Takemura, K., Sone, S., Yabuta, H., Sato, K., Tamura, T., Nakajima, K., Ohnishi, S., Tokashiki, K., Hyashi, Y., Kato, Y., Miyasaka, Y., Yoshida, M., and Ono, H., A stacked capacitor technology with ECR plasma MOCVD (Ba,Sr)TiO_3 and RuO_2/Ru/TiN/$TiSi_x$ strorage nodes for Gb-scale DRAM's, *IEEE Trans. Electron Devices*, **44** (1997) 1076–1081.
64. Kim, H. W. and Kang, C.-J., Investigation into patterning of stack-type Ru electrode capacitor, *Microelectron. Eng.*, **69** (2003) 89–96.
65. Kim, H.-W., Ju, B.-S., Kang, C.-J., and Moon, J.-T., A study on the Pt electrode etching for 0.15 μm technologies, *Microelectron. Eng.*, **65** (2003) 185–195.
66. Mainka, G., Beitel, G., Schnabel, R.F., Saenger, A., and Dehm, C., Chemical mechanical polishing of iridium and iridium oxide for damascene processes, *J. Electrochem. Soc.*, **148** (2001) G552–G558.

67. Lee, W.-J. and Park, H.-S., Development of novel process for Ru CMP using ceric ammonium nitrate (CAN)-containing nitric acid, *Appl. Surf. Sci.*, **228** (2004) 410–417.
68. Yoo, W. J., Hahm, J. H., Kim, H. W., Jung, C. O., Koh, Y. B., and Lee, M. Y., Control of etch slope during etching of Pt in $Ar/Cl_2/O_2$ plasmas, *Jpn. J. Appl. Phys.*, **35** (1996) 2501–2504.
69. Chung, C. W., Kim, H. I., and Song, Y. S., High-density plasma etching of iridium thin films in a $Cl_2/O_2/Ar$ plasma, *J. Electrochem. Soc.*, **150** (2003) G297–G299.
70. Saito, S., and Kuramasu, K., Plasma etching of RuO_2 thin films, *Jpn. J. Appl. Phys.*, **31** (1992) 135–138.
71. Haisma, J., Spierings, G. A. C. M., Michielsen, T. M., and Adema, C. L., Surface aspects and phenomenological aspects of direct bonding, *Philips. J. Res.*, **49** (1995) 23–46.
72. Evans, D. R., Chemically active slurry for the polishing of noble metals and method for the same, *U.S. Patent*, US6290736 (2001).
73. Tsai, M. S., Sun, S. C., and Tseng, T.-Y., Effect of bottom electrode materials on the electrical and reliability characteristics of $(Ba,Sr)TiO_3$ capacitors, *IEEE Trans. Electron Devices*, **46** (1999) 1829–1838.
74. Kishiro, K., Inoue, N., Chen, S.-C., and Yoshimaru, M., Structure and electrical properties of thin Ta_2O_5 deposited on metal electrodes, *Jpn. J. Appl. Phys.*, **37** (1998) 1336–1339.
75. Aoyama, T., Yamazaki, S., and Imai, K., Ultrathin Ta_2O_5 film capacitor with Ru bottom electrode, *J. Electrochem. Soc.*, **145** (1998) 2961–2964.
76. Joshi, P. C. and Cole, M. W., Influence of postdeposition annealing on the enhanced structural and electrical properties of amorphous and crystalline Ta_2O_5 thin films for dynamic random access memory applications, *J. Appl. Phys.*, **86** (1999) 871–880.
77. Lin, J., Masaaki, N., Tsukune, A., and Yamada, M., Ta_2O_5 thin films with exceptionally high dielectric constant, *Appl. Phys. Lett.*, **74** (1999) 2370–2372.
78. Lee, J. W., Song, H. S., Kim, K. M., Lee, J. M., and Roh, J. S., The physical and electrical characteristics of Ta_2O_5 and physical vapor deposited Ru in metal-insulator-metal capacitors, *J. Electrochem. Soc.*, **149** (2002) F56–F62.
79. Kim, J.-W., Nam, S.-D., Lee, S.-H., Won, S.-J., Kim, W.-D., Yoo, C.-Y., Park, Y.-W., Lee, S.-I., and Lee, M.-Y., Development of $Ru/Ta_2O_5/Ru$ capacitor technology for giga-scale DRAMs, *Int. Electron. Device Meet. Tech. Dig.*, (1999) 793–796.
80. Dietz, G. W., Schumacher, M., Waser, R., Streiffer, S. K., Basceri, C., and Kingon, A. I., Leakage currents in $Ba_{0.7}Sr_{0.3}TiO_3$ thin films for ultrahigh-density dynamic random access memories, *J. Appl. Phys.*, **82** (1997) 2359–2364.
81. Hwang, C. S., Lee, B. T., Kang, C. S., Kim, J. W., Lee, K. H., Cho, H.-J., Horii, H., Kim, W. D., Lee, S. I., Roh, Y. B., and Lee, M. Y., A comparative study on the electrical conduction mechanisms of $(Ba_{0.5}Sr_{0.5})TiO_3$ thin films on Pt and IrO_2 electrodes, *J. Appl. Phys.*, **83** (1998) 3703–3713.
82. Yoon, D.-S. and Roh, J. S., Thin Pt layer insertion into the Ru bottom electrode: effects on the surface morphplogy of a $(Ba, Sr)TiO_3$ dielectric film and on the performance of the TiN barrier in the Pt/Ru/TiN/p-Si/Si heterostructure, *Semicond. Sci. Technol.*, **17** (2002) 1048–1057.
83. Hong, S., Bak, H., An, I., and Kim, O. K., Microstructural and electrical properties of $Ba_xSr_{1-x}TiO_3$ thin films on various electrodes, *Jpn. J. Appl. Phys.*, **39** (2000) 1796–1800.

84. Lee, J. M., Kang, S. Y., Shin, J. C., Kim, W. J., Hwang, C. S., and Kim, H. J., Improvements in electrical properties of (Ba,Sr)TiO_3 capacitor with chemical vapor deposited Pt top electrode using Pt hexafluoroacetylacetonate, *Appl. Phys. Lett.*, **74** (1999) 3489–3491.
85. Jeon, Y.-C., Seon, J.-M., Joo, J.-H., Oh, K.-Y., Roh, J.-S., Kim, J.-J., and Kim, D.-S., Thermal stability of Ir/polycrystalline-Si structure for bottom electrode of integrated ferroelectric capacitors, *Appl. Phys. Lett.*, **71** (1997) 467–469.
86. Aoyama, T., Yamazaki, S., and Imai, K., Characteristics of (Ba, Sr)TiO_3 capacitors with textured Ru bottom electrode, *Jpn. J. Appl. Phys.*, **39** (2000) 6348–6357.
87. Joo, J.-H., Seon, J.-M., Jeon, Y.-C., Oh, K.-Y., Roh, J.-S., Kim, J.-J., and Choi, J.-T., Investigation of ruthenium electrodes for (Ba,Sr)TiO_3 thin films, *Jpn. J. Appl. Phys.*, **37** (1998) 3396–3401.
88. Yoon, D.-S., Hong, K., and Roh, J. S., Process window extension of TiN diffusion barrier using preoxidation of Ru and RuO_x film for (Ba,Sr)TiO_3 dielectric film, *J. Vac. Sci. Technol. A*, **19** (2001) 1730–1736.
89. Kawahara, T., Yamamuka, M., Yuuki, A., and Ono, K., (Ba, Sr)TiO_3 films prepared by liquid source chemical vapor deposition on Ru electrodes, *Jpn. J. Appl. Phys.*, **35** (1996) 4880–4885.
90. Ahn, J.-H., Choi, W.-Y., Lee, W.-J., and Kim, H.-G., Annealing of RuO_2 and Ru bottom electrodes and its effect on the electrical properties of (Ba,Sr)TiO_3 thin films, *Jpn. J. Appl. Phys.*, **37** (1998) 284–289.
91. Tarutani, M., Yamamuka, M., Takenaga, T., Kuroiwa, T., and Horikawa, T., Improved fabrication process for Ru/BST/Ru capacitor by liquid source chemical vapor deposition, *Thin Solid Films*, **409** (2002) 8–14.
92. Kil, D.-S., Park, J.-B., Yoon, D.-S., Song, C.-R., Cho, H. J., Kim, Y., Yu, Y.-S., Roh, J.-S., and Yoon, H.-K., Leakage current characteristics of (Ba,Sr)TiO_3 thin films deposited on Ru electrodes prepared by metal organic chemical vapor deposition, *Jpn. J. Appl. Phys.*, **40** (2001) 3260–3265.
93. Aoyama, T., Murakoshi, A., and Imai, K., Ru electrode deposited by sputtering in Ar/O_2 mixture ambient, *Jpn. J. Appl. Phys.*, **37** (1998) 5701–5707.
94. Chen, T.-S., Balu, V., Katakam, S., Lee, J.-H., and Lee, J. C., Effects of Ir electrodes on barium strontium titanate thin-film capacitors for high-density memory application, *IEEE Trans. Electron. Dev.*, **46** (1999) 2304–2309.
95. Cha, S. Y., Jang, B.-T., and Lee, H. C., Effects of Ir electrodes on the dielectric constants of $Ba_{0.5}Sr_{0.5}TiO_3$ films, *Jpn. J. Appl. Phys.*, **38** (1999) L49–L51.
96. Cho, H.-J., Kang, C. S., Hwang, C. S., Kim, J.-W., Horii, H., Lee, B. T., Lee, S. I., and Lee, M. Y., Structural and electrical properties of $Ba_{0.5}Sr_{0.5}TiO_3$ films on Ir and IrO_2 electrodes, *Jpn. J. Appl. Phys.*, **36** (1997) L874–L876.
97. Saenger, K. L., Grill, A., and Cabral, Jr., C., Noble metal silicide formation in metal/Si structures during oxygen annealing: Implications for perovskite-based memory devices, *J. Mater. Res.*, **13** (1998) 462–468.
98. Shimizu, M., Hyodo, S., Fujisawa, H., Niu, H., and Shiosaki, T., Step coverage characterization of Pb(Zr, Ti)O_3 thin films on various electrode materials by metalorganic chemical vapor deposition, *Jpn. J. Appl. Phys.*, **36** (1997) 5808–5811.
99. Fox, G. R., Chu, F., and Davenport, T., Current and future ferroelectric nonvolatile memory technology, *J. Vac. Sci. Technol. B*, **19** (2001) 1967–1971.
100. Takasu, H., Ferroelectric memories and their applications, *Microelectron. Eng.*, **59** (2001) 237–246.

101. Kim, K. and Song, Y. J., Integration technology for ferroelectric memory devices, *Microelectron. Reliab.*, **43** (2003) 385–398.
102. Paz de Araujo, C. A., Solayappan, N., McMillan, L. D., Otsuki, T., and Arita, K., Process integration of embedded FeRAMs, *J. Electroceramics*, **3** (1999) 135–142.
103. Zambrano, R., Applications and issues for ferroelectric NVMs, *Mater. Sci. Semicond. Process.*, **5** (2003) 305–310.
104. Ishiwara, H., Recent progress of ferroelectric memories, *Int. J. High Speed Electron. Syst.*, **12** (2002) 315–323.
105. Miller, S. L. and McWhorter, Physics of the ferroelectric nonvolatile memory field effect transistor, *J. Appl. Phys.*, **72** (1992) 5999–6010.
106. Pinnow, C.-U. and Mikolajick, Material aspects in emerging nonvolatile memories, *J. Electrochem. Soc.*, **151** (2004) K13–K19.
107. Park, B. H., Kang, B. S., Bu, S. D., Noh, T. W., Lee, J., and Jo, W., Lanthanum-substituted bismuth titanate for use in non-volatile memories, *Nature*, **401** (1999) 682–684.
108. Chou, H.-Y., Chen, T.-M., and Tseng, T.-Y., Electrical and dielectric properties of low-temperature crystallized $Sr_{0.8}Bi_{2.6}Ta_2O_{9+x}$ thin films on $Ir/SiO_2/Si$ substrates, *Mater. Chem. Phys.*, **82** (2003) 826–830.
109. Lee, J.-M., Kim, K.-T., and Kim, C.-I., Structural and electrical properties of metal-ferroelectric-insulator-semiconductor field-effect transistors using a $Pt/Bi_{3.25}La_{0.75}Ti_3O_{12}/CeO_2/Si$ structure, *Thin Solid Films*, **447–448** (2004) 332–326.
110. Tagantsev, A. K., Stolichnov, I., Colla, E. L., and Setter, N., Polarization fatigue in ferroelectric films: Basic experimental findings, phenomenological scenarios, and microscopic features, *J. Appl. Phys.*, **90** (2001) 1387–1402.
111. Lee, J. K., Park, Y., and Chung, I., Investigation of hydrogen induced degradation in $Pb(Zr_xTi_{1-x})O_3$ thin film capacitors for the application of memory devices, *J. Appl. Phys.*, **92** (2002) 2724–2728.
112. Matsui, Y., Suga, M., Hiratani, M., Miki, H., and Fujisaki, Y., Oxygen diffusion in Pt bottom electrodes of ferroelectric capacitors, *Jpn. J. Appl. Phys.*, **36** (1997) L1239–L1241.
113. Nakamura, T., Nakao, Y., Kamisawa, A., and Takasu, H., Preparation of $Pb(Zr,Ti)O_3$ thin films on electrodes including IrO_2, *Appl. Phys. Lett.*, **65** (1994) 1522–1524.
114. Jones, Jr. R. E., Integration of ferroelectric nonvolatile memories, *Solid State Technol.*, **40(10)** (1997) 201–210.
115. Nam, H.-J., Choi, D.-K., and Lee, W.-J., Formation of hillocks in Pt/Ti electrodes and their effects on short phenomena of PZT films deposited by reactive sputtering, *Thin Solid Film*, **371** (2000) 264–271.
116. Al-Shareef, H. N., Bellur, K. R., Kingon, A. I., and Auciello, O., Influence of platinum interlayers on the electrical properties of $RuO_2/Pb(Zr_{0.53}Ti_{0.47})O_3/RuO_2$ capacitor heterostructures, *Appl. Phys. Lett.*, **66** (1995) 239–241.
117. Asano, G., Morioka, H., Funakubo, H., Shibutami, T., and Oshima, N., Fatigue-free $RuO_2/Pb(Zr,Ti)O_3/RuO_2$ capacitor prepared by metalorganic chemical vapor deposition at 395 °C, *Appl. Phys. Lett.*, **83** (2003) 5506–5508.
118. Lee, H.-C. and Lee, W.-J., Preparation and characterization of $Pb(Zr,Ti)O_3$ films deposited on Pt/RuO_2 hybrid electrode for ferroelectric random access memory devices, *Jpn. J. Appl. Phys.*, **40** (2001) 6566–6573.

119. Ramesh, R., Aggarwal, S., and Auciello, O., Science and technology of ferroelectric films and heterostructures for non-volatile ferroelectric memories, *Mater. Sci. Eng. R*, **32** (2001) 191–236.
120. Park, Y., and Song, J. T., Characteristics of $Pb(Zr,Ti)O_3$ thin films deposited on Ru/RuO_2 double layer, *Mater. Lett.*, **58** (2004) 2128–2131.
121. Lee, H.-C. and Lee, W.-J., Characterization of $Pb(Zr, Ti)O_3$ thin films fabricated by plasma enhanced chemical vapor deposition on Ir-based electrodes, *J. Vac. Sci. Technol. A*, **20** (2002) 1939–1947.
122. Lee, M.-S., Park, K.-S., Nam, S.-D., Lee, K.-M., Seo, J.-S., Joo, S.-H., Lee, S.-W., Jung, Y.-J., Heo, J.-E., Park, S.-O., Chung, U-I., and Moon, J.-T., Integration of ferroelectric random access memory devices with $Ir/IrO_2/Pb(Zr_xTi_{1-x})O_3/Ir$ capacitors formed by metalorganic chemical vapor deposition-grown $Pb(Zr_xTi_{1-x})O_3$, *Jpn. J. Appl. Phys.*, **41** (2002) 6709–6713.
123. Asano, G., Oikawa, T., Funakubo, H., and Saito, K., Good ferroelectricity of $Pb(Zr,Ti)O_3$ thin films fabricated by highly reproducible deposition on bottom Ir electrode at 395 °C, *Jpn. J. Appl. Phys.*, **42** (2003) L1083–L1086.
124. Bernstein, S. D., Wong, T. Y., Kisler, Y., and Tstison, R. W., Fatigue of ferroelectric $PbZr_xTi_yO_3$ capacitors with Ru and RuO_x electrodes, *J. Mater. Res.*, **8** (1993) 12–13.
125. Bandaru, J., Sands, T., and Tsakalakos, L., Simple Ru electrode scheme for ferroelectric $(Pb,La)(Zr,Ti)O_3$ capacitors directly on silicon, *J. Appl. Phys.*, **84** (1998) 1121–1125.
126. Liu, K.-S., Tseng, T.-F., and Lin, I-N., Improvement of $(Pb_{1-x}La_x)(Zr_yTi_{1-y})_{1-x/4}O_3$ ferroelectric thin films by use of $SrRuO_3/Ru/Pt/Ti$ bottom electrodes, *Appl. Phys. Lett.*, **72** (1998) 1182–1184.
127. Maiwa, H., Ichinose, N., and Okazaki, K., Preparation and properties of Ru and RuO_2 thin film electrodes for ferroelectric thin films, *Jpn. J. Appl. Phys.*, **33** (1994) 5223–5226.
128. Johnson, J. A., Lisoni, J. G., and Wouters, D. J., Developing a conductive oxygen barrier for ferroelectric integration, *Microelectron. Eng.*, **70** (2003) 377–383.
129. Watts, B. E., Leccabue, F., Guerri, S., Severi, M., Fanciulli, M., Ferrari, S., Tallarida, G., and Morandi, C., A comparison of Ti/Pt and TiN/Pt electrodes used with ferroelectric $SrBi_2Ta_2O_9$ films, *Thin Solid Films*, **406** (2002) 23–29.
130. Kim, J.-W., Choi, J.-H., and Oh, T.-S., Electrical characteristics of $Sr_xBi_{2.4}Ta_2O_9$ thin film and $Pt/Sr_{0.85}Bi_{2.4}Ta_2O_9/Al_2O_3/Si$ structure, *J. Mater. Sci.*, **38** (2003) 1853–1857.
131. Moon, B.-K., Isobe, C., Hironaka, K., and Hishikawa, S., Effect of interfacial layers on dielectric properties in very thin $SrBi_2Ta_2O_9$ capacitors, *J. Appl. Phys.*, **89** (2001) 6557–6559.
132. Kweon, S. Y., Choi, S. K., Yang, W. S., Yeom, S. J., and Roh, J. S., Stacked $Pt/SrBi_2Ta_{2-x}Nb_xO_9/Pt/IrO_x/Ir$ capacitor on poly plug, *Jpn. J. Appl. Phys.*, **41** (2002) 66–69.
133. Kim, K.-T. and Kim, C.-I., Effect of $Bi_4Ti_3O_{12}$ seeding layer on the structural and ferroelectric properties of $Bi_{3.25}La_{0.75}Ti_3O_{12}$ thin films fabricated by a metalorganic decomposition method, *Thin Solid Films*, **447–448** (2004) 413–417.
134. Sato, T., Kuroiwa, T., Sugahara, K., and Ishiwara, H., Preparation of $Bi_{3.25+x}La_{0.75}TiO_{12+y}$ films on ruthenium electrodes, *Jpn. J. Appl. Phys.*, **41** (2002) 2105–2109.
135. Kweon, S. Y., Kim, N. K., Choi, E. S., Yeom, S. J., Roh, J. S., and Park, Y. J., Ohmic contact properties of tungsten plug and ferroelectric properties of $(Bi,La)_4TiO_3O_{12}$ thin film in stacked capacitor structure, *Jpn. J. Appl. Phys.*, **41** (2002) 7327–7331.
136. Wilk, G. D., Wallace, R. M., and Anthony, J. M., High-κ gate dielectrics: current status and materials properties considerations, *J. Appl. Phys.*, **89** (2001) 5243–5275.

137. Schaeffer, J. K., Samavedam, S. B., Gilmer, D. C., Dhandapani, V., Tobin, P. J., Mogab, J., Nguyen, B.-Y., White, Jr. B. E., Dakshina-Murthy, S., Rai, R. S., Jiang, Z.-X., Martin, R., Raymond, M. V., Zavala, M., La, L. B., Smith, J. A., Garcia, R., Roan, D., Kottke, M., and Gregory, R. B., Physical and electrical properties of metal gate electrodes on HfO_2 gate dielectrics, *J. Vac. Sci. Technol. B*, **21** (2003) 11–17.
138. Youm, M., Sim, H. S., Jeon, H., Kim, S.-I., and Kim, Y. T., Metal oxide semiconductor field effect transistor characteristics with iridium gate electrode on atomic layer deposited ZrO_2 high-*k* dielectrics, *Jpn. J. Appl. Phys.*, **42** (2003) 5010–5013.
139. Misra, V., Zhong, H., and Lazar, H., Electrical properties of Ru-based alloy gate electrodes for dual metal gate Si-CMOS, *IEEE Electron Dev. Lett.*, **23** (2002) 354–356.
140. Tsui, B.-Y. and Huang, C.-F., Wide range work function modulation of binary alloys for MOSFET application, *IEEE Electron Dev. Lett.*, **24** (2003) 153–155.
141. Schaeffer, J. K., Fonseca, L. R. C., Samavedam, S. B., Liang, Y., Tobin, P. J., and White, B. E., Contributions to the effective work function of platinum on hafnium dioxide, *Appl. Phys. Lett.*, **85** (2004) 1826–1828.
142. Hooker, J. C., Aaltonen, T., Alén, P., Ritala, M., Leskelä, M., Roozeboom, F., van den Heuvel, E., van Zilj, J., Maas, M. M., and Raymakers, T., Work function evaluation of noble metal gate electrodes deposited by atomic layer deposition on hafnium oxide: platinum, iridium and ruthenium, *ALD 2004*, Helsinki, August 16-18 (2004).
143. Papadatos, F., Skordas, S., Consiglio, S., Kaloyeros, A. E., and Eisenbraun, E., Characterization of ruthenium and ruthenium oxide thin films deposited by chemical vapor deposition for CMOS gate electrode applications, *Mat. Res. Soc. Symp. Proc.*, **745** (2003) 61–66.
144. Zhu, W. J., Ma, T.-P., Tamagawa, T., Kim, J., and Di, Y., Current transport in metal/hafnium oxide/silicon structure, *IEEE Electron Dev. Lett.*, **23** (2002) 97–99.
145. Dey, S. K., Goswami, J., Gu, D., de Waard, H., Marcus, S., and Werkhoven, C., Ruthenium films by digital chemical vapor deposition: selectivity, nanostructure, and work function, *Appl. Phys. Lett.*, **84** (2004) 1606–1608.
146. Ťapajna, M., Písečny, P., Lupták, R., Hušeková, K., Frölich, K., Harmatha, L., Hooker, J. C., Roozeboom, F., and Jergel, J., Application of Ru-based gate materials for CMOS technology, *Mater. Sci. Semicond. Process.*, **7** (2004) 271–276.
147. Mao, A. Y., Sun, Y. M., White, J. M., and Kwong, D. L., Thermal and chemical instability between iridium gate electrode and Ta_2O_5 gate dielectric, *Mat. Res. Soc. Symp. Proc.*, **567** (1999) 489–494.
148. Pawlak, M. A., Schram, T., Maex, K., and Vantomme, A., Investigation of iridium as a gate electrode for deep sub-micron CMOS technology, *Microelectron. Eng.*, **70** (2003) 373–376.
149. Fillot, F., Chenevier, B., Maîtrejean, S., Audier, M., Chaudouët, P., Bochu, B., Sénateur, J. P., Pisch, A., Mourier, T., Monchoix, H., Guillaumot, B., and Passemard, G., Investigations of the interface stability in HfO_2–metal electrodes, *Microelectron. Eng.*, **70** (2003) 384–391.
150. Nam, S.-W., Yoo, J.-H., Nam, S., Ko, D.-H., Yang, C.-W., and Ku, J.-H., Characteristics of ZrO_2 films with Al and Pt gate electrodes, *J. Electrochem. Soc.*, **150** (2003) G849–G853.
151. Choi, K.-J. and Yoon, S.-G., Characteristics of Pt and TaN metal gate electrode for high-κ hafnium oxide gate dielectrics, *Electrochem. Solid-State Lett.*, **7** (2004) G47–G49.

152. Zhong, H., Heuss, G., Suh, Y.-S., Misra, V., and Hong, S.-N., Electrical properties of Ru and RuO_2 gate electrodes for Si-PMOSFET with ZrO_2 and Zr-silicate dielectrics, *J. Electron. Mater.,* **30** (2001) 1493–1498.
153. Zhong, H., Heuss, G., Misra, V., Luan, H., Lee, C.-H., and Kwong, D.-L., Characterization of RuO_2 electrodes on Zr silicate and ZrO_2 dielectrics, *Appl. Phys. Lett.*, **78** (2001) 1134–1136.
154. Chyan, O., Arunagiri, T. N., and Ponnuswamy, T., Electrodeposition of copper thin film on ruthenium – a potential diffusion barrier for Cu interconnects, *J. Electrochem. Soc.*, **150** (2003) C347–C350.
155. Josell, D., Wheeler, D., Witt, C., and Moffat, T. P., Seedless superfill: copper electrodeposition in trenches with ruthenium barriers, *Electrochem. Solid-State Lett.*, **6** (2003) C143–C145.
156. Kwon, O.-K., Kim, J.-H., Park, H.-S., and Kang, S.-W., Atomic layer deposition of ruthenium thin films for copper glue layer, *J. Electrochem. Soc.*, **151** (2004) G109–G112.
157. Lane, M. W., Murray, C. E., McFeely, F. R., Vereecken, P. M., and Rosenberg, R., Liner materials for direct electrodeposition of Cu, *Appl. Phys. Lett.*, **83** (2003) 2330–2332.
158. Josell, D., Moffat, T. P., Aaltonen, T., Ritala, M., and Leskelä, M., unpublished results.
159. Chan, R., Arunagiri, T. N., Zhang, Y., Chyan, O., Wallace, R. M., Kim, M. J., and Hurd, T. Q., Diffusion studies of copper on ruthenium thin film: A plateable copper diffusion barrier, *Electrochem. Solid-State Lett.*, **7** (2004) G154–G157.
160. Kim, J. J., Kim, S.-K., and Kim, Y. S., Direct plating of low resistivity bright Cu film onto TiN barrier layer via Pd activation, *J. Electrochem. Soc.*, **151** (2004) C97–C101.
161. Wang, Z., Yaegashi, O., Sakaue, H., Takahagi, T., and Shingubara, S., Highly adhesive electroless Cu layer formation using an ultra thin ionized cluster beam (ICB)-Pd catalytic layer for sub-100 nm Cu interconnections, *Jpn. J. Appl. Phys.*, **42** (2003) L1223–L1225.
162. Elers, K.-E., Saanila, V., Soininen, P. J., Li, W.-M., Kostamo, J. T., Haukka, S., Juhanoja, J., and Besling, W. F. A., Diffusion barrier deposition on a copper surface by atomic layer deposition, *Chem. Vap. Deposition*, **8** (2002) 149–153.
163. Rossnagel, S. M. and Kuan, T. S., Alteration of Cu conductivity in the size effect regime, *J. Vac. Sci. Technol. B*, **22** (2004) 240–247.
164. Goswami, I. and Laxman, R., Transition metals show promise as copper barriers, *Semicond. Inter.*, **27(5)** (2004) 49–54.
165. Rahtu, A., Alaranta, T., and Ritala, M., In situ quartz crystal microbalance and quadrupole mass spectrometry studies of atomic layer deposition of aluminum oxide from trimethyl aluminum and water, *Langmuir*, **17** (2001) 6506–6509.
166. Aarik, J., Aidla, A., Jaek, A., Kiisler, A.-A., and Tammik, A.-A., Properties of amorphous Al_2O_3 films grown by ALE, *Acta Polytech. Scand., Chem. Technol. Metall. Ser.*, **195** (1990) 201–208.
167. Chason, E. and Mayer, T. M., Thin film and surface characterization by specular X-ray reflectivity, *Crit. Rev. Solid State Mater. Sci.*, **22** (1997) 1–67.
168. van der Lee, A., Grazing incidence specular reflectivity: theory, experiment, and applications, *Solid State Sci.*, **2** (2000) 257–278.
169. Fuchs, E., Oppolzer, H., and Rehme, H., *Particle Beam Microanalysis, Fundamentals, Methods and Applications*,VCH, Weinheim, (1990), 227–276.
170. Goldstein, J. I., Newbury, D. E., Echlin, P., Joy, D. C., Romig, Jr, A. D., Lyman, C. E., Fiori, C., and Lifshin, E., *Scanning Electron Microscopy and X-Ray Microanalysis*, 2nd ed., Plenum Press, New York, (1992), 778–781.

171. Waldo, R. A., An iteration procedure to calculate film compositions and thicknesses in electron-probe microanalysis, *Microbeam Anal.*, **23** (1988) 310–314.
172. Jokinen, J., Keinonen, J., Tikkanen, P., Kuronen, A., Ahlgren, T., and Nordlund, K., Comparison of TOF-ERDA and nuclear resonance reaction techniques for range profile measurements of keV energy implants, *Nucl. Instrum. Methods Phys. Res., Sect. B*, **119** (1996) 533–542.
173. Jokinen, J., Haussalo, P., Keinonen, J., Ritala, M., Riihelä, D., and Leskelä, M., Analysis of AlN thin films by combining TOF-ERDA and NRB techniques, *Thin Solid Films*, **289** (1996) 159–165.
174. Reeves, G. K., Lawn, M. W., and Elliman, R. G., Resistivity measurements of thin film iridium on silicon, *J. Vac. Sci. Technol. A*, **10** (1992) 3203–3206.
175. Kwon, O.-K., Kwon, S.-H., Park, H.-S., and Kang, S.-W., Plasma-enhanced atomic layer deposition of ruthenium thin films, *Electrochem. Solid-State Lett.*, **7** (2004) C46–C48.
176. Min, Y.-S., Bae, E. J., Jeong, K. S., Cho, Y. J., Lee, J.-H., Choi, W. B., and Park, G.-S., Ruthenium oxide nanotube arrays fabricated by atomic layer deposition using carbon nanotube template, *Adv. Mater.*, **15** (2003) 1019–1022.
177. Senkevich, J. J., Tang, F., Rogers, D., Drotar, J. T., Jezewski, C., Lanford, W. A., Wang, G.-C., and Lu, T.-M., Substrate-independent palladium atomic layer deposition, *Chem. Vap. Deposition*, **9** (2003) 258–264.
178. Marsh, E. P. and Uhlenbrock, S., Process for low temperature atomic layer deposition of Rh, *U.S. Patent*, US20036656835 (2003).
179. Kuzmina, N., Paramonov, S., Ivanov, R., Kezko, V., Polamo, K., and Troyanov, S., Silver pivalate as a new volatile precursor for thin film deposition, *J. Phys. IV*, **9** (1999) Pr8-923– Pr8-928.
180. Igumenov, I. K., MO CVD of noble metals, *J. Phys. IV*, **5** (1995) C5-489–C5-496.
181. Chi, Y., Yu, H.-L., Ching, W.-L., Liu, C.-S., Chen, Y.-L., Chou, T.-Y., Peng, S.-M., and Lee, G.-H., Deposition of osmium thin films using pyrazolate complexes as CVD source reagents, *J. Mater. Chem.*, **12** (2002) 1363–1369.
182. Green, M. L., Gross, M. E., Papa, L. E., Schnoes, K. J., and Brasen, D., Chemical vapor deposition of ruthenium and ruthenium dioxide films, *J. Electrochem. Soc.*, **132** (1985) 2677–2685.
183. *The Chemistry of Metal CVD*, (Ed: T. Kodas and M. J. Hampden-Smith), VCH, Weinheim, Germany (2002).
184. Maury, F. and Senocq, F., Iridium coatings grown by metal-organic chemical vapor deposition in a hot-wall CVD reactor, *Surf. Coat. Technol.*, **163–164** (2003) 208–213.
185. Garcia, V. J. R. and Goto, T., Chemical vapor deposition of iridium, platinum, rhodium and palladium, *Mater. Trans., JIM*, **44** (2003) 1717–1728.
186. Hierso, J.-C., Feurer, R., and Kalck, P., Platinum, palladium and rhodium complexes as volatile precursors for depositing materials, *Coord. Chem. Rev.*, **178–180** (1998) 1811–1834.
187. Kim, Y., Method for fabrication ruthenium thin layer, *U.S. Patent Application*, US2002173054 (2002).
188. Lashdaf, M., Hatanpää, T., and Tiitta, M., Volatile β-diketonato complexes of ruthenium, palladium and platinum. Preparation and thermal characterization, *J. Therm. Anal.Calorim.*, **64** (2001) 1171–1182.
189. Kukli, K., Aaltonen, T., Aarik, J., Lu, J., Ritala, M., Ferrari, S., Hårsta, A., and Leskelä, M., Atomic layer deposition and characterization of HfO_2 films on noble metal substrates, *J. Electrochem. Soc.*, in press.

190. Matsui, Y., Hiratani, M., Nabatame, T., Shimamoto, Y., and Kimura, S., Growth mechanism of Ru films prepared by chemical vapor deposition using bis(ethylcyclopentadienyl)ruthenium precursor, *Electrochem. Solid-State Lett.*, **4** (2001) C9–C12.
191. Lee, J.-H., Kim, J.-Y., and Rhee, S.-W., Chemical vapor deposition of RuO_2 thin films using the liquid precursor $Ru(OD)_3$, *Electrochem. Solid-State Lett.*, **2** (1999) 622–623.
192. Utriainen, M., Kröger-Laukkanen, M., Johansson, L.-S., and Niinistö, L., Studies of metallic thin film frowth in an atomic layer epitaxy reactor using $M(acac)_2$ (M = Ni, Cu, Pt) precursors, *Appl. Surf. Sci.*, **157** (2000) 151–158.
193. Xue, Z., Thridandam, H., Kaesz, H. D., and Hicks, R. F., Organometallic chemical vapor deposition of platinum. Reaction kinetics and vapor pressures of precursors, *Chem. Mater.*, **4** (1992) 162–166.
194. Kukli, K., Aaltonen, T., Uustare, T., Aarik, J., Ritala, M., and Leskelä, M., unpublished results.
195. Morozova, N. B., Semyannikov, P. P., Sysoev, S. V., Grankin, V. M., and Igumenov, I. K., Saturated vapor pressure of iridium(III) acetylacetonate, *J. Therm. Anal. Cal.*, **60** (2000) 489–495.
196. Siedle, A. R., Newmark, R. A., and Pignolet, L. H., Structure of palladium bis(hexafluoroacetylacetonate) and the systematics of its acid-base chemistry, *Inorg. Chem.*, **22** (1983) 2281–2286.
197. Liu, Y.-H., Cheng, Y.-C., Tung, Y.-L., Chi, Y., Chen, Y.-L., Liu, C.-S., Peng, S.-M., and Lee, G.-H., Synthesis and characterization of fluorinated β-ketoiminate and imino-alcoholate Pd complexes: precursors for palladium chemical vapor deposition, *J. Mater. Chem.*, **13** (2003) 135–142.
198. Marsh, E. P. and Uhlenbrock, S., Process for direct deposition of ALD RhO_2, *U.S. Patent Application*, US2003233976 (2003).
199. Collins, J. E., Castellani, M. P., Rheingold, A. L., Miller, E. J., Geiger, W. E., Rieger, A. L., and Rieger, P. H., Synthesis, characterization, and molecular structure of bis(tetraphenylcyclopentadienyl)-rhodium(II), *Organometallics*, **14** (1995) 1232–1238.
200. Sheldrick, G. M., *SHELXTL Reference Manual*, Version 5.1., Bruker AXS Inc., Madison, Wisconsin, USA (1997).
201. Kwon, O.-K., Kwon, S.-H., Park, H.-S., and Kang, S.-W., PEALD of a ruthenium adhesion layer for copper interconnects, *J. Electrochem. Soc.*, **151** (2004) C753–C756.
202. Kreuzer, H. J., Payne, S. H., Drozdowski, A., Menzel, D., Theory of dissociative and nondissociative adsorption and desorption, *J. Chem. Phys.*, **110** (1999) 6982–6999.
203. Rotermund, H. H., Lauterbach, J., and Haas, G., The formation of subsurface oxygen on Pt(100), *Appl. Phys. A*, **57** (1993) 507–511.
204. von Oertzen, A., Mikhailov, A., Rotermund, H.-H., and Ertl, G., Subsurface oxygen formation on the Pt(110) surface: experiment and mathematical modeling, *Surf. Sci.*, **350** (1996) 259–270.
205. Marinova, Ts. S. and Kostov, K. L., Interaction of oxygen with a clean Ir(111) surface, *Surf. Sci.*, **185** (1987) 203–212.
206. Leisenberger, F. P., Koller, G., Sock, M., Surnev, S., Ramsey, M. G., Netzer, F. P., Klötzer, B., and Hayek, K., Surface and subsurface oxygen on Pd(111), *Surf. Sci.*, **445** (2000) 380–393.
207. Voogt, E. H., Mens, A. J. M., Gijzeman, O. L. J., and Geus, J. W., Adsorption of oxygen and surface oxide formation on Pd(111) and Pd foil studied with ellipsometry, LEED, AES, and XPS, *Surf. Sci.*, **373** (1997) 210–220.
208. Peterlinz, K. A. and Sibener, S. J., Absorption, adsorption, and desorption studies of the oxygen/Rh(111) system using O_2, NO, and NO_2, *J. Phys. Chem.*, **99** (1995) 2817–2825.